Title: A novel method for reliably measuring miniature and spontaneous postsynaptic potentials/currents in whole-cell patch clamp recordings in the central nervous system

Abbreviated Title: Novel method for measuring mPSPs/mPSCs in the CNS

Author Names and Affiliations: Martynas Dervinis[1,2], Guy Major[1]

[1]: School of Biosciences, Cardiff University, Cardiff, Wales, CF10 3AT, UK

[2]: Department of Neuroscience, University of Copenhagen, Blegdamsvej 3, DK-2200 Copenhagen, Denmark

Corresponding author email address: martynas.dervinis@gmail.com

Number of pages: 64

Number of figures: 15

Number of words:

Abstract: 229

Introduction: 649

Discussion: 1492

Conflict of interest statement: The authors declare no competing financial interests.

27 **Acknowledgements**: Cardiff University (GM, MD), The Medical Research Council of the UK (MD PhD)

28

Abstract

In chemical synapses of the central nervous system (CNS), information is transmitted via the presynaptic release of a vesicle (or 'quantum') of neurotransmitter, which elicits a postsynaptic electrical response with an amplitude termed the 'quantal size'. This key determinant of neural computation is hard to measure reliably due to its small size and the multiple sources of noise within neurons and electrophysiological recordings. Measuring amplitudes of miniature postsynaptic currents (mPSCs) or potentials (mPSPs) at the cell soma potentially offers a technically straightforward way to estimate quantal sizes, as each of these miniature responses (or 'minis') is elicited by the spontaneous release of a single neurotransmitter vesicle. However, a somatically recorded mini is typically massively attenuated compared with at its input site, and a significant fraction are indistinguishable from (or cancelled out by) background noise fluctuations. For minis to be accurately estimated, the noise component would need to be characterised independently. As the first step in devising such a method, we developed and described a novel mPSP/mPSC detection algorithm as part of our quantal analysis software called 'minis'. We tested its performance in detecting simulated minis in whole-cell recordings from pyramidal neurons in rat neocortical slices and compared it to two of the most-used mini detection algorithms. This benchmarking revealed superior detection by our algorithm. The release version of the algorithm also offers great flexibility via graphical and programming interfaces.

Significance statement

Accurately measuring the range of electrical ‘sizes’ of synapses in the brain is critical for understanding neural computations. As an important first step, we introduce a novel algorithm for detecting voltage or current transients (‘minis’) resulting from synapses spontaneously releasing vesicles containing neurotransmitters. We objectively evaluate this algorithm and compare it to other popular algorithms used for detecting spontaneous synaptic responses, setting an important methodological standard. Because of its superior performance and flexibility, our algorithm also offers a useful technological improvement for synapse researchers. The evaluation process we use highlights common methodological pitfalls bedevilling spontaneous synaptic signalling research, and points to potential solutions.

59 # Abbreviations

60 aCSF – artificial cerebrospinal fluid

61 AMPA – α-amino-3-hydroxy-5-methyl-4-isoxazolepropionic acid

62 AP – action potential

63 API - application programming interface

64 AUC – area under the curve

65 CNS – central nervous system

66 CPP – (*RS*)-3-(2-carboxypiperazin-4-yl)-propyl-1-phosphonic acid

67 d' – sensitivity index 'd-prime' (defined in Methods)

68 FNR – false negative rate ('miss' rate)

69 FPR – false positive rate ('false alarm' rate)

70 GABA – gamma-aminobutyric acid

71 IPSC – inhibitory post-synaptic current

72 IPSP – inhibitory post-synaptic potential

73 mEPSC– miniature excitatory post-synaptic current

74 mEPSP– miniature excitatory post-synaptic potential

75 mIPSC– miniature inhibitory post-synaptic current

76 mIPSP– miniature inhibitory post-synaptic potential

77 mPSC – miniature post-synaptic current

78 mPSP – miniature post-synaptic potential

NBQX – 2,3-dioxo-6-nitro-1,2,3,4-tetrahydrobenzo[*f*]quinoxaline-7-sulfonamide

NMDA – N-methyl-D-aspartate

ROC – receiver operator characteristic

sEPSC– spontaneous excitatory post-synaptic current

sEPSP– spontaneous excitatory post-synaptic potential

sIPSC– spontaneous inhibitory post-synaptic current

sIPSP– spontaneous inhibitory post-synaptic potential

smEPSC – simulated mEPSC

smEPSP – simulated mEPSP

smPSC – simulated mPSC

smPSP – simulated mPSP

sPSC – spontaneous post-synaptic current

sPSP – spontaneous post-synaptic potential

TNR – true negative rate

TPR – true positive rate ('hit' rate, sensitivity)

TTX – tetrodotoxin

V_m – membrane potential

v-ROC – virtual ROC (ROC-like plot)

Introduction

Synaptic transmission in the CNS occurs in 'quanta' (Kuno, 1964; Larkman et al., 1991; Kraszewski and Grantyn, 1992; Kullmann and Nicoll, 1992; Stern et al., 1992; Jonas et al., 1993; Isaacson and Walmsley, 1995; Forti et al., 1997; Wall and Usowicz, 1998; Sahara and Takahashi, 2001; Hardingham et al., 2010) usually thought to correspond to the release of a single neurotransmitter vesicle (Heuser et al., 1979). The amplitude of the postsynaptic response to a quantum of transmitter, the quantal size, is a key parameter defining the efficacy of synaptic transmission (Vere-Jones, 1966; Katz, 1969) and, therefore, an important determinant of neural computation.

Quantal size measurements in the CNS are difficult due to multi-synaptic contacts, limited accessibility, significant quantal variance, temporal non-stationarity of synaptic properties, and low signal-to-noise ratios of somatic electrophysiological recordings of quantal events (Korn and Faber, 1991; Bekkers, 1994). For these reasons classical quantal analysis as done at the neuromuscular junction has run into problems in central synapses. More recent methods such as noise deconvolution, Variance-Mean analysis, and optical quantal analysis have not fared much better either (Edwards et al., 1976; Jack et al., 1981; Redman, 1990; Clamann et al., 1991; Reid and Clements, 1999; Yuste et al., 1999; Clements and Silver, 2000; Oertner et al., 2002; Clements, 2003; Silver, 2003; Biró et al., 2005; Enoki et al., 2009; Peled and Isacoff, 2011; Liu et al., 2022).

A complementary method of assessing synaptic function is to measure properties of mPSCs. Miniature PSC amplitude measurements are often taken as quantal size estimates across the population of active synapses onto a neuron, as the mPSC (under voltage clamp) or mPSP (under voltage recording) likely correspond to the response to a spontaneous release of a single neurotransmitter vesicle (Fatt and Katz, 1952; del Castillo and Katz, 1954; Brown et al., 1979; Isaacson and Walmsley, 1995; Wall and Usowicz, 1998). Measurements of mPSC amplitudes are

122 routine in the literature. However, they are likely overestimates due to small amplitude events being
123 difficult to detect and largely being missed.
124
125 The use of voltage clamp can be a major reason why mPSCs “go missing”. Theoretical studies (Rall
126 and Segev, 1985; Major, 1993; Spruston et al., 1993) predicted and experimental findings (Williams
127 and Mitchell, 2008) confirmed that voltage clamp fails to clamp extended dendrites, and to capture
128 the current flowing in at electrically remote synapses. Amplitude attenuation can also be caused if
129 series resistance is not compensated (Williams and Mitchell, 2008). These issues can be somewhat
130 sidestepped by switching to voltage recording.
131
132 However, most mPSCs go undetected because of the electrophysiology of the neuron itself. Distal
133 minis leak charge via the dendritic membrane, but an even more significant amplitude attenuation,
134 40-fold or more, is inflicted by charging the membrane capacitance of dendritic trees (Stuart and
135 Spruston, 1998; Williams and Stuart, 2002; Nevian et al., 2007; Williams and Mitchell, 2008; Larkum
136 et al., 2009; Major et al., 2013). Such amplitudes, at the soma, are often indistinguishable from noise
137 fluctuations. Recording from thin dendrites close to synaptic input sites is technically challenging
138 (Nevian et al. 2007). Therefore, a reliable yet widely accessible quantal analysis method, based on
139 somatic whole-cell patch recording, would require taking account of the background noise
140 component in addition to measuring putative mPSPs (or mPSCs).
141
142 As an initial step in creating such a method, we developed a novel algorithm, called ‘minis’, to detect
143 miniature (and action potential-triggered) postsynaptic events. A novel algorithm was needed for
144 several reasons. Firstly, existing algorithms have not been described in sufficient detail in the peer-
145 reviewed literature. Popular algorithms like Mini Analysis and Clampfit are proprietary. Secondly,
146 because existing algorithms are not open, they are not modifiable. Thus, they cannot be automated
147 and integrated with other software. Lastly, existing algorithms have not yet, to our knowledge, been

benchmarked in peer-reviewed articles. To fill these gaps, we developed an algorithm that is transparent, flexible, open-source, and objectively evaluated using standardised criteria.

Materials and Methods

Published values for amplitudes and frequencies of minis.

We searched the neuroscience literature between January 1, 2020 – January 31, 2022 for a representative sample of recently reported amplitudes and frequencies of miniature excitatory postsynaptic currents (mEPSCs) and potentials (mEPSPs) in cortical pyramidal cells, and common data analysis practices in the CNS. We also compared reported mEPSC rates per second to a predicted range of values. We limited our search to publications in English only that reported research results on synaptic function in the CNS. We examined the title and abstract fields of studies in MEDLINE database using the PubMed search engine with the following search keywords: ("spontaneous neurotransmission" OR "spontaneous neurotransmitter release" OR "spontaneous transmitter release" OR "spontaneous postsynaptic" OR "miniature postsynaptic" OR "mEPSP" OR "mEPSC" OR "mPSP" OR "mPSC" OR "mIPSP" OR "mIPSC" OR OR "sEPSP"[Title/Abstract] OR "sEPSC"[Title/Abstract] OR "sPSP"[Title/Abstract] OR "sPSC"[Title/Abstract] OR "sIPSP"[Title/Abstract] OR "sIPSC"[Title/Abstract]) AND ("cortex"[Title/Abstract] OR "cortical"[Title/Abstract] OR "neocortex"[Title/Abstract] OR "neocortical"[Title/Abstract] OR "hippocampus"[Title/Abstract] OR "hippocampal"[Title/Abstract] OR "thalamus"[Title/Abstract] OR "thalamic"[Title/Abstract] OR "brain"[Title/Abstract] OR "cerebral"[Title/Abstract] OR "central nervous system"[Title/Abstract] OR "pyramidal"[Title/Abstract] OR "CNS"[Title/Abstract]). Abbreviations ending in PSP and PP stand for postsynaptic potentials, while PSC and PC stand for postsynaptic currents and should not be confused with end-plate potentials and currents.

Animals and electrophysiology

All experimental procedures were carried out in accordance with the UK Animals (Scientific Procedures) Act 1986 at Cardiff University under Home Office personal and project licenses.

176 19 to 27-day old Wistar rats (RRID:RGD_13508588; n = 11) of either sex were anaesthetised with
177 isoflurane and decapitated, and the brain removed under cold (0-2 °C) artificial cerebrospinal fluid
178 (aCSF), composed of (in mM) 125 NaCl, 26 $NaHCO_3$, 2.3 KCl, 1.26 KH_2PO_4, 1 $MgSO_4$, 10 glucose, and 2
179 $CaCl_2$ bubbled with 95% O_2 5%CO_2. Coronal somatosensory cortical slices 350 µm thick were cut and
180 held in an interface chamber with their surfaces kept moist for 1 to 3 hours by aCSF at room
181 temperature (21-23°C) under a 95% O_2 5% CO_2 atmosphere. Individual slices were then placed in the
182 recording chamber and held at 35-37°C with aCSF flowing over both surfaces. For recording
183 purposes at 35-37°C the aCSF solution contained (in mM) 125 NaCl, 24 $NaHCO_3$, 2.3 KCl, 1.26 KH_2PO_4,
184 1 $MgSO_4$, 10 glucose, and 2 $CaCl_2$.
185
186 Whole-cell recordings (n = 14) were obtained under visual control using infrared scanning gradient
187 contrast imaging with the imaging laser beam and a Dodt tube. Recordings were made with 4.5-9
188 MΩ borosilicate glass pipettes (Harvard Apparatus, 1.5 mm outside diameter and 0.86 mm, internal
189 diameter, omega-dot filament; Sutter P2000 puller), filled with (mM): 140 KGluconate, 10 HEPES, 2
190 $MgCl_2$, 3 ATP-Na_2, 0.3 GTP-Na, 0.1 Magnesium Green, 0.1 Alexa 594; 7.35 pH, 273 mOsm/L
191 osmolarity. Signals were amplified, low-pass filtered (5 KHz) and digitised (Axopatch-200B, custom
192 amplifier/filters, Digidata 1440, Clampex software; Molecular Devices). Pipettes and electrodes were
193 positioned with Sutter MP265 and 285 manipulators with a diagonal (axial) mode, using
194 parallelogram trajectories.
195
196 The electrophysiological recordings consisted of two phases. During the first phase we recorded
197 mEPSPs against the background of physiological noise ('noise + minis' condition) by applying aCSF
198 with action potential and inhibitory postsynaptic potential blockers added: 0.5 or 1 µM tetrodotoxin
199 (TTX; selective, potent Na^+ channel blocker), and 12.5 µM gabazine (selective, potent $GABA_A$
200 receptor antagonist to block (fast components) of inhibitory synaptic inputs – IPSCs and resulting
201 IPSPs). Action potential (AP) blockade by TTX was explicitly tested for with long current pulses

202 pushing membrane potential (V_m) well above normal AP threshold levels, to around -20 mV. The
203 average duration of this phase of the recordings was 21.8 (± s.d. 0.9) minutes. During a second
204 phase, we recorded noise with mEPSPs blocked ('noise-alone' condition). This recording was carried
205 out after further adding 40 µM 2,3-dioxo-6-nitro-7-sulfamoyl-benzo[f]quinoxaline (NBQX) (selective,
206 potent α-amino-3-hydroxy-5-methyl-4-isoxazolepropionic acid (AMPA) receptor antagonist) and 50
207 µM CPP (competitive, non-use dependent selective N-methyl-D-aspartate (NMDA) receptor
208 antagonist) to the solution used in the 'noise + minis' condition, to block all excitatory glutamatergic
209 synaptic inputs (and thus EPSPs), verified by inspecting and analysing the traces across a number of
210 recordings with the same flow rates. The average duration of this phase of the recordings was 44.8
211 (± s.d. 2.9) minutes.
212
213 **Experimental design**
214 The goal of this benchmarking study was to compare mEPSP detection performance by three
215 different detection algorithms, mainly in terms of standard signal detection theory measures. Two of
216 them were the most popular software products used in the field of synaptic function research in the
217 CNS, while the third one was our novel algorithm called 'minis'.
218
219 Current clamp whole-cell patch recordings obtained during the initial recording phase ('noise +
220 minis' condition) were not used in this benchmarking study. The current clamp recordings obtained
221 during the second recording phase ('noise-alone' condition) served as the background data in the
222 mEPSP ('simulated minis') computer simulations (n=14 cells). Computationally simulated mEPSPs
223 (smEPSPs) were added onto segments of these V_m noise recordings (2 of them 200 seconds, while
224 the remaining 12 were 100 seconds long) and the resultant hybrid waveforms (noise + simulated
225 minis) were then subjected to mEPSP detection analyses using 'minis', Mini Analysis (Bluecell;
226 RRID:SCR_002184), and Clampfit (part of the pClamp software suite, Molecular Devices;

227 RRID:SCR_011323) software. Detection performance was quantified using signal detection theory
228 measures and compared between the three algorithms.
229
230 **Simulations**
231 *Simulating distributions of miniature excitatory postsynaptic potentials with a range of amplitudes*
232 *and rise times*
233 All simulations were carried out within the 'minis' software environment which is based on Matlab
234 (Mathworks; RRID:SCR_001622). Simulation of minis-like events was based on an analytical solution
235 to the passive cable equation for a transient current (Rall, 1977) using 100 lumped terms with a
236 double exponential synaptic current with τ_1= 0.1 ms and τ_2 = 2 ms (Major et al., 1993).
237
238 For a given membrane time constant, an initial cable segment was constructed with an electrotonic
239 length l/λ = 0.6, where l is the physical length of a dendrite (µm) and λ is the length (µm) constant
240 (Rall, 1977). Charge (Q) was injected at a location (x µm) along this cable and the resulting simulated
241 postsynaptic V_m was measured at one end of this cable segment. The precise location of the injected
242 charge was varied systematically, depending on the desired shape of the simulated event. Increasing
243 the distance of the injected charge along the cable away from the measurement site gradually
244 increased the rise time of the simulated event. To further increase the rise time, electrotonic length
245 was gradually increased until the required rise time was obtained. Increasing the amount of injected
246 charge increased the amplitude of the simulated event. Therefore, one was able to construct a
247 simulated postsynaptic potential of any rise time or amplitude, for the particular membrane time
248 constant used. A pool of simulated events could be created having any kind of distribution of
249 amplitudes and rise times, for a given decay time constant, with individual events' onsets
250 timed/placed pseudo-randomly along the time axis of the V_m recording.
251

Simulations used to construct full receiver operating characteristic (ROC)-like curves, using relatively fixed but realistic ('moderately-sized') mini amplitudes

All simulated mEPSPs were drawn from a two-dimensional normal distribution (independent amplitude and rise time dimensions) with the following amplitude parameters: mean μ_1 = 0.3 mV and standard deviation σ_1 = 0.05 mV (i.e., amplitudes relatively constant, with a relatively small amount of variation). The following (independent) 10-90% rise time parameters were used: μ_2 = 0.05 ms and σ_2 = 2.5 ms (with a minimum rise time of 0.05 ms; i.e., only upper half of normal distribution used). Simulated events were drawn pseudo-randomly from a distribution at one of the following frequencies (minis/second): 640, 320, 160, 80, 40, 20, 10, 5, 2.5, 2.5, 2.5, 2.5, 2.5, and 2.5. Corresponding noise amplitude scale factors for these 14 frequency conditions were as follows: 1, 1, 1, 1, 1, 1, 1, 1, 1, 1.2, 1.4, 1.8, 2.6, and 4.2. The simulated events were then positioned at pseudo-randomly determined times along the V_m noise recording epochs obtained during the second recording phase ('noise-alone' condition). Two of the noise-alone epochs were 200 seconds long, while the remaining twelve were 100 seconds long. Four different simulation traces per recording, each of them having different pseudo-random event timings, were generated for every frequency/noise scale condition, resulting in a total number of 14×4×14 = 784 traces.

Simulations of miniature excitatory postsynaptic potentials using a range of biologically realistic amplitudes at realistic frequencies

The simulation parameters used to construct full ROC-like curves cover only a part of the likely biological range. In reality, in cortex, minis vary far more in their amplitudes, with large numbers of smaller minis, but a minority of bigger minis too - some much bigger. Therefore, we set out to compare all three algorithms using a range of plausible simulated mini amplitudes, within the restricted range of what we deemed to be realistic frequencies based on our estimation (from recent peer-reviewed publications) in the first Results subsection.

All simulated events were drawn from a two-dimensional distribution with the following parameters: amplitudes were chosen from twelve discrete values (0.05, 0.1, 0.15, 0.2, 0.25, 0.3, 0.35, 0.4, 0.45, 0.5, 0.55 and 0.6 mV) with equal probabilities, rise times were independently chosen from the upper half of a normal distribution with mean μ_2 = 0.05 ms, and standard deviation σ_2 = 2.5 ms (i.e., no rise time shorter than 0.05 ms). Three 'realistic' mini frequencies were used: either 53, 33, or 13 minis/s. The simulated events were positioned at pseudo-random times along the same noise recording epochs as used in the previous subsection. Four different simulation traces per recording, each of them with different random event timings, were generated for every frequency condition, resulting in a total number of 3×4×14 = 168 traces.

Detection of spontaneous and miniature postsynaptic potentials

'minis' detection algorithm

We developed a new algorithm to detect postsynaptic potentials and currents, that we have incorporated into a data analysis software package called 'minis', coded in Matlab (Mathworks). It is distributed as an application programming interface (API) in the form of a packaged Matlab app or a Python (Python Software Foundation; RRID:SCR_008394) package or as a compiled standalone desktop application with a graphical user interface. In brief, the detection algorithm takes a filtered V_m or clamp current trace in the Axon Binary File (ABF) format and detects peaks and rising phases and estimates their amplitudes and rise and decay times after applying certain processing steps. These steps are outlined below (with parameter values tailored for detecting smEPSPs in cortical pyramidal neurons). A schematic illustration of the key steps is shown in Figure 1:

A. Steps to find minis:

1. The data can be band-stop filtered to remove mains noise (e.g., small integer multiples of 50 Hz frequency components: optional). For this, a Butterworth filter (Matlab's 'butter' function) is used with a stopband attenuation of 10 dB and a passband 'ripple' of 0.05 dB.

303 The stopband size is 1 Hz, and the passband is the entire remaining frequency range except
304 for the ±3 Hz window either side of the stopband frequency.
305 2. The recording trace can be smoothed using a Gaussian window (optional). We use a 1.5-
306 millisecond window (with standard deviation of the Gaussian of 0.53 ms). This step removes
307 high frequency noise.
308 3. Peaks (local maxima) are identified in the filtered, smoothed recording trace. Each peak is
309 then examined consecutively, starting with the initial peak.
310 4. Going through all the peaks one by one, any peak within the "Peak Integration Period"
311 ('duration') following the current ('working') peak of interest is discarded if it is *smaller*
312 (lower) than the peak of interest. For the analysis in this paper, we use a Peak Integration
313 Period of 2.5 ms; this can be matched to the different 'sharpnesses' or 'breadths' of peaks
314 in different data.
315 5. If there is a larger peak within the peak integration period, the 'working' peak of interest is
316 moved to this new peak, and the old peak and all intervening peaks between it and the new
317 'working' peak of interest are discarded.
318 6. The baseline of the peak is positioned asymmetrically around the lowest value (local
319 minimum) before the peak. Because of the faster upstroke of minis, compared with their
320 decays, 80% of the baseline period falls before the lowest voltage (local minimum) and the
321 remaining 20% after it (see Figure 1, inset). The interval from the baseline to the peak is
322 limited by the *Maximum Time-to-Peak* parameter (10 ms used here). The last 20% of the
323 baseline cannot start earlier than this.
324 7. The length in time of the baseline is controlled by the *baseline duration* parameter. We
325 used 2-ms. (N.B. a baseline, or indeed an entire mini, can occur during the summated decay
326 'tails' of previous minis, particularly when the minis frequency is high relative to their decay
327 time, as often seen with mPSPs under voltage recording at body temperature – but also
328 under voltage clamp).

8. If the baseline overlaps with or falls before the previous peak, its start is delayed till immediately after the previous peak (to stop the baseline being pulled down by the previous rising phase), but the end time is kept the same.
9. To reject any large artefactual 'glitches', or small events that are putative noise, if the amplitude of the peak is outside of the range of acceptable amplitudes, between a detection threshold and a maximum, the peak is discarded. We allowed a range of amplitudes of 0.1-10 mV in detection conditions used to construct full 'virtual' receiver operating characteristic (ROC) curves. In other conditions we applied a range of 0.05-10 mV. (N.B. 0.02 or 0.03 mV detection thresholds are useful for real whole-cell patch recording data from neocortical pyramidal neurons, under our experimental conditions, guided by the range of amplitudes of dendritically detected, somatically recorded mEPSPs in Nevian et al. (2007) from layer 5 pyramidal neurons from rat somatosensory cortex; in general, detection thresholds will need to be adjusted to the cell type and experimental conditions).

B. Steps against multiple small minis being erroneously lumped together (merged):

10. Rising phase asymmetries: if the first half of the rise time (10-50% or 20-50%, depending on the rise time duration of choice) is longer than the second half (50-90% or 50-80%) by a factor of 5 or more (an asymmetry incompatible with typical single, non-summating EPSP or EPSC rising phases), the end of the baseline is extended slightly into the 'take-off' of the rising phase. (This correction can be repeated one more time).
11. The amplitude range test is applied again (Step 9).
12. If the second half of the rise time is longer than the first half by a factor of 5 or more, the peak is shifted to a previously discarded smaller peak, if exists. (Two minis could be summating on their rising phases, which is treated as a single mini, or the second mini could occur just after the peak of the first, which is treated as two minis, if two peaks are distinguishable).
13. The amplitude range test is applied again (Step 9).

14. If the 10% or 20% rise time mark (depending on whether 10-90% or 20-80% rise time is measured) is later than the end of the baseline by more than a half of the baseline duration (1 ms in our case), a new baseline is established closer to the peak (by moving the baseline to the next local minimum).
15. Finally, the amplitude range test is applied again (Step 9).
16. A mini (mPSP/mPSC) is established.

Detection using Mini Analysis software

Mini Analysis software version 6.0.7 was used to detect mEPSPs for a benchmarking purpose. We used the following detection parameters: As with the 'minis' program, an amplitude threshold of 0.1 mV (when constructing the full ROC-like curve) or 0.05 mV (all other simulated conditions), in both cases somewhat matched to the simulated data, a "Period to search for a Local maximum" of 12.5 ms, "Time before a peak for baseline" of 10 ms, a "Period to search a decay time" of 30 ms, a "Fraction of peak to find a decay time" of 0.37 (one effective time constant for exponential decay), a "Period to average a baseline" of 2 ms, an "Area threshold" of 0 mV×ms (i.e., not used), a "Number of points to average for peak" of 1, and using the "Detect complex peak" option (to avoid missing close-together events). The chosen detection parameters closely resembled similarly named parameters in the 'minis' detection algorithm with minor deviations to improve performance. Arrived by trial and error, these parameters were also found to give the most optimal detection performance of the Mini Analysis software in comparison to other tested parameter sets. Event detection was carried out on the recording data that was filtered and smoothed in the same way as described in steps 1 and 2 of the previous sub-section.

Detection using Clampfit

Clampfit software, part of the pClamp 11.0.3.03 software suite, was used to detect real and simulated mEPSPs and mEPSCs for a benchmarking purpose. Recordings were band-stop filtered as

381 described in step 1 of the 'minis' detection algorithm. Data was not smoothed. A template search
382 algorithm was used with 9 templates. The mEPSP template set was constructed based on the
383 simulated events. Events having 0.5 ms, 1.5 ms, 3.5 ms, and 6.5 ms 10-90% rise times were selected
384 to produce 4 distinct mEPSP templates (with the correct decay time constants). An additional 5
385 single-peaked templates were constructed in a way that made them potentially a mix of multiple
386 simulated waveforms. They were constructed to have extra-fast, fast, intermediate, slow, and extra-
387 slow rise times corresponding to 2 ms, 2.75 ms, 6 ms, 7 ms, and 8 ms 0-100% rise times and 8 ms,
388 9.25 ms, 17 ms, 23 ms, and 37 ms duration full decays, respectively. Combining single and mixed
389 waveforms gave better detection performance than having waveforms based only on any one of
390 these types alone. Template match threshold was set to the default of 4 noise standard deviations
391 with the rest of the detection parameters being set to their default values as well. The same set of
392 templates was used to analyse all simulated current clamp data.
393
394 *Detection algorithm response classification*
395 At the outset we identified prominent noise events in the V_m noise recordings (the 2nd recording
396 phase: 'noise-alone' condition) that could potentially be confused for true minis (mEPSPs) by any of
397 the algorithms (noise traces in Figures 2A and B). All noise recordings were filtered and smoothed as
398 in Steps 1 and 2 of the 'minis' detection algorithm. The data was further smoothed by a rectangular
399 'box-car' moving average window of 20 ms. Then all peaks larger than 0.01 mV and having a half-
400 width of at least 0.5 ms were identified. These peaks were classed as (notional) noise 'events' (for
401 the purpose of generating 'sensible' true negative rates, TNRs, which do not 'swamp' false positive
402 rates across the entire virtual ROC; see below). Subsequently we simulated mEPSPs and added them
403 at pseudo-random times to a zero-trace having the same length as the noise recording of interest
404 (Simulation traces in Figures 2A and B). The peaks of these events were classed as signal events. The
405 simulated trace was then added to the noise recording ("Simulation + noise" traces in Figures 2A and
406 B). Locations of signal and designated noise events formed the 'ground truth' information.

407

408 Following the detection process, all detected events were associated with one of the signal and
409 noise events depending on their proximity to these predefined 'ground truth' events. A detected
410 event was classed as a true positive (a 'hit') if it was the closest detection event within 5ms of a
411 signal (simulated mEPSP/mini) event. If no detection event occurred within the 10 ms symmetrical
412 window surrounding a signal (simulated mini) event (-5 to 5 ms), the signal event was classed as a
413 false negative (a 'miss'). If no detection event (except correct detections) occurred within the same
414 duration window surrounding a noise event, the noise event was classed as a true negative ('correct
415 rejection'). Although in theory there could potentially be a much higher number of possible time
416 points which could be labelled as correct rejections, or true negatives, in this situation, because of
417 their inherently somewhat arbitrary nature, we wanted to keep the maximum number comparable
418 to the maximum number of true positives (simulated minis), so the ROC plot had a reasonable
419 chance of being relatively 'square' (i.e. having a useful dynamic range). The remaining detection
420 events were classed as false positives ('false alarms'). Examples of classified detection events are
421 shown in Figure 2 separately for all three detection algorithms.

422

423 *Detection response time to the nearest neighbour*

424 The time to the peak of the nearest smEPSP was available for every classified response. Detection
425 performance was then evaluated as a function of the time to the nearest neighbour.

426

427 **Membrane potential 'phase' (trend) classification**

428 We attempted to address common detection errors, in particular missed minis on the decaying
429 phase of a previous mini (causing second peak to drop relative to its baseline), or on the rising phase
430 of another mini (so the rises of both minis get lumped together). Algorithm detection performance
431 was assessed not only for full recordings but also separately for periods when the 'underlying'
432 simulated V_m (before adding the noise) was rising, decaying, or remained roughly stable (Figure 3).

433 The 'decaying phases' (downward trend) of the purely simulated V_m were set to be a) the period
434 from 0.0625 ms after the peak until the purely simulated V_m trace dropped to the ratio of 0.3/e mV
435 (0.11 mV) (amplitudes of simulated minis were ~0.3 mV in the full virtual-ROC curve conditions, so
436 this would be about one membrane time constant after an 'average' simulated mini) or b) until the
437 V_m started rising again to reach a new peak that was above the initial peak (at the start of this decay
438 phase). If the new peak was lower than the initial one, the entire new peak was classified as part of
439 the ongoing decay phase. Peaks occurring on the decay phase of the V_m were assigned the V_m decay
440 rate of change that was present 0.25 ms (5 sample points) prior to the appearance of the V_m
441 inflection points associated with the start of the rise of a new mini (indicated by the blue arrow in
442 Figure 3A). The rising 'phase' was treated essentially somewhat as a decay phase in reverse. The only
443 difference was that the ratio of 0.3/e mV was replaced by the ratio of 0.3/10 mV (0.03 mV). Peaks
444 occurring on a V_m rise phase (upward trend) were assigned a V_m rate of rise value that was present
445 0.125 ms *after* the appearance of an upward V_m inflection point following the initial decay of the
446 previous peak (indicated by green arrows in Figure 3A). Periods that were already classified as decay
447 phases could not be reclassified as rising phases. Periods of relatively slowly-changing simulated V_m,
448 outside of the rise and decay phases were classed as "stable" (or a flattish phase). The classification
449 of purely simulated membrane potentials into three different trend phases was used to assign
450 phases to the combined noise recordings + simulated minis (Figure 3B). The detection performance
451 during rise and decay trend phases was evaluated as a function of the V_m rate of change.
452
453 **Data Analyses**
454 Performance of the three algorithms was compared using measures from signal detection theory. All
455 detection responses were classified as described in the *Detection algorithm response classification*
456 subsection. True positive ('hit') rate (TPR) was calculated as follows:
457 $$TPR = \frac{True\ positive\ count}{True\ positive\ count + False\ negative\ count}.$$
458

Throughout this text we use TPR, detection probability, and sensitivity interchangeably. False positive ('false alarm') rate (FPR) was calculated as follows:

$$FPR = \frac{False\ positive\ count}{False\ positive\ count + True\ negative\ count}.$$

The true negative count we have used is perforce notional, as explained above, but still useful for standardised, non-subjective comparisons and benchmarking. Throughout we use FPR and 'false alarm rate' interchangeably.

Calculation of TPR and (notional) FPR allowed us to produce ROC-like curves and to calculate area under the curve (AUC; area under the ROC curve, for each complete ROC curve, with 0.5 indicating chance performance (the area of the triangle under the diagonal from (0,0) to (1,1) and 1 indicating perfect performance, i.e., the area of a right angle starting at (0,0), vertical to (0,1) then going horizontal to (1,1)) as detection performance indicators. These are the most commonly used performance indicators for classifiers, in addition to sensitivity (TPR), and d' (discriminability or sensitivity index) which we often use in parallel throughout this text. The d' statistic was calculated as follows:

$$d' = z(TPR) - z(FPR),$$

where z is the z-score defined as the inverse of the normal cumulative distribution function, i.e. z(arg) is the number of sd's from the mean giving the area equal to its argument arg under the standard unit normal distribution (mean 0, sd 1), starting from -∞. TPR and FPR values are essentially treated as cumulative probabilities as explained in (Macmillan and Creelman, 2005). So d' tells us how many standard deviations 'apart' the TPR and FPR are, assuming they are cumulative probabilities (areas under curve) of a standard normal distribution. N.B. If FPR is 0, z(FPR) is -∞ so d' is undefined, but arbitrarily large and positive (as occurs in some of our figures below). These plots

are truncated for the detection method in question, but the performance is still superior to any plots with finite values.

The above detection performance indicators were calculated for full recordings, as well as separately for rising and decaying periods of V_m.

In addition, we also looked at cumulative (left-to-right over the x-axis) TPR and cumulative FPR. The cumulative TPR was defined as follows, for each detection algorithm and simulated waveform:

$$Cumulative\ TPR = \frac{Cumulative\ true\ positive\ count}{Total\ unbanded\ true\ positive\ count} * Overall\ unbanded\ TPR.$$

Likewise, the cumulative FPR was defined as:

$$Cumulative\ FPR = \frac{Cumulative\ false\ positive\ count}{Total\ unbanded\ false\ positive\ count} * Overall\ unbanded\ \ FPR.$$

The latter two measures were not only useful for measuring cumulative hits and false alarms over a range of time intervals and V_m rates of change, but also provided overall estimates of TPR and FPR.

Statistical analyses

All inferential statistics were based on the assumption that distributions of all measures were normal. All mean distribution values are stated/depicted with 95% confidence limits of the mean.

Data accessibility

All data analysed in this study is publicly available (Dervinis, 2023a). The available data include 'noise-alone' whole-cell patch membrane potential recordings that were used in computer simulations. The hybrid V_m traces containing smEPSPs added to noise recordings are also available. All electrophysiological recordings were stored in Axon Binary File (ABF) format.

507 mEPSP templates used for detecting real and simulated events via Clampfit are also in the same
508 dataset in the form of Axon Template Files (ATFs).
509
510 **Code accessibility**
511 All analyses were carried out in Matlab and the analysis code is publicly available on GitHub
512 (Dervinis, 2023b). The code is complete with instructions on how to reproduce all figures reported in
513 this study.
514
515 **Software accessibility**
516 The present study reported the use of a novel mEPSP/mEPSC detection algorithm that is part of
517 'minis' open-source software available on GitHub (Dervinis, 2023c).
518

Results

Research literature measuring minis in the central nervous system

There were 107 studies in total that matched our criteria. All of these studies used voltage clamp as the electrophysiological method for recording spontaneous and miniature postsynaptic events. We surveyed the software they used to detect these events. The biggest group, ~48%, reported using Mini Analysis. 26% reported using Clampfit, while 13% used a custom algorithm. The remaining 13% did not specify. We compared the performance of the two most popular detection algorithms, Mini Analysis and Clampfit, both commercially available, with our new algorithm 'minis'.

35 studies (ca. 32%) reported using a current amplitude detection threshold of which 19 studies specified actual numeric value used (-6.8 ± s.d. 0.44 pA, range of -3 to -20 pA). It is likely that a higher fraction of studies made use of amplitude thresholds as only two explicitly reported not using any detection thresholds. Most of the studies did not give enough details (65% of all studies) to judge one way or the other. However, studies that used Mini Analysis for detection must have used a detection threshold, as this software requires it.

Out of all the studies, 18 carried out research in neocortical pyramidal cells looking at mPSCs only (spontaneous PSCs excluded). 12 studies reported a mean mEPSC amplitude value of -11.74 ± s.d. 0.77 pA (range of -6.0 to -20.9 pA). 13 studies reported a mean frequency value of 3.6 ± s.d. 0.34 per second (range of 1.0 to 8.0 per second).

The total putative excitatory synapse count on a single cortical pyramidal cell can number in the tens of thousands (Eyal et al., 2018b). Layer 2/3 pyramidal cells in rats are thought to have 5,000 to 30,000 putative excitatory synapses (Larkman, 1991; Eyal et al., 2018b). Large-thick-trunk/tufted layer 5 pyramidal cells would have an even larger number of contacts (Larkman, 1991). Therefore,

544 we can roughly assume that for most cortical pyramidal cells the number of putative excitatory
545 synapses ranges between 5,000 and 50,000. Conservatively, we could assume that only a minority,
546 roughly 40%, of them are functional ('non-silent') synapses with active zones and post-synaptic
547 densities containing AMPA receptors (Motta et al., 2019; Holler et al., 2021). Given that a
548 spontaneous vesicle release at a single release site has been estimated to occur with an approximate
549 frequency of 0.0021 per second (Murthy and Stevens, 1999) and given that there may be at least 2.7
550 release sites per cortical synapse (Holler et al., 2021), the lower bound frequency estimate of such
551 events within a single cortical pyramidal neuron might be expected to range somewhere between
552 ca. 10 minis/s and 100 minis/s (5,000*0.4*0.0021*2.7– 50,000*0.4*0.0021*2.7). Frequency values
553 reported in the recent literature are below this predicted range by an order of magnitude,
554 suggesting a significant fraction of smaller minis may commonly be 'missed' under some recording
555 conditions. This problem has been observed directly (Nevian et al., 2007), using paired dendritic and
556 somatic whole-cell patch recordings, albeit using voltage recording rather than voltage clamp,
557 recording from large layer 5 neocortical pyramidal neurons.
558
559 **Algorithm performance comparison for detecting moderately-sized (~0.3 mV) simulated miniature**
560 **excitatory postsynaptic potentials**
561 *Detection under a wide range of frequency conditions: overall performance*
562 In the Results subsection 'Research literature measuring minis in the central nervous system', we
563 reported that detection of spontaneous postsynaptic events is typically carried out using an
564 amplitude threshold. This approach implies that the range of amplitudes of spontaneous
565 postsynaptic events is somewhat known and that, on the smaller end, the amplitudes are
566 moderately-sized and sufficiently larger than pure noise fluctuations. Leaving aside the question of
567 the empirical validity of this (somewhat dubious?) assumption, we evaluated automated detection
568 of moderately-sized (0.3 ± s.d. 0.05 mV) smEPSPs added to whole-cell patch clamp noise recordings
569 (the 2nd recording phase: 'noise-alone' condition).

We compared our novel ‘minis’ algorithm with Mini Analysis and Clampfit. We created 14 simulation frequency conditions with different effective signal-to-noise ratios that loosely mimicked the effects of varying the signal detection threshold. On the one hand, increasing the frequency of smEPSPs tended to decrease TPR as simulated events started to merge. On the other hand, increasing the noise amplitude (scaling up the noise that was added to the simulated minis) tended primarily to increase the FPR.

We plotted the detection performance in terms of TPRs against FPRs, as ‘virtual’ (notional) Receiver Operator Characteristic (v-ROC) curves, for all 14 conditions and all three algorithms in Figure 4A. We found that in the first six conditions (high minis frequencies), the v-ROC curve for ‘minis’ had minimal overlap with any other curve and was positioned furthest away from the diagonal (starting from left to right; 640, 320, 160, 80, 40, and 20 minis/s with x1 noise scaling), indicative of a superior performance in this (relatively high) frequency range (the highest frequencies were used to create the full v-ROC; higher frequencies increase overlaps, i.e. temporal summation, between minis, which are particularly challenging to detect). The same observation was supported by another measure, the sensitivity index d’, shown in Figure 4B. Detection performance in the remaining 8 conditions (10, 5, 2.5, 2.5, 2.5, 2.5, 2.5, and 2.5 minis/s with noise scaling factors of x 1, 1, 1, 1.2, 1.4, 1.8, 2.6, and 4.2, respectively) was very similar for both ‘minis’ and Mini Analysis: neither of the two showed a clear superiority on both performance measures simultaneously: v-ROC and d’ curves overlapped. In contrast, Clampfit consistently performed worst across all 14 conditions, particularly with high amplitude noise. Clampfit becomes progressively ‘confused’ as noise increases, placing templates on noise events, but ignoring ‘swamped’ smEPSPs.

When overall performance was assessed averaging across individual frequency and signal-to-noise ratio conditions, we found that ‘minis’ showed the best performance with the mean Area Under the

596 (v-ROC) Curve (AUC) value of 0.960 ± 0.002 (95% confidence interval here onwards; Figure 4C). A
597 paired samples t-test comparing to Mini Analysis which had a mean AUC value of 0.937 ± 0.0022
598 gave t(13) = 12.4 and p = 1.37×10^{-8}. Clampfit showed the poorest overall performance with the mean
599 AUC value of 0.706 ± 0.0043, t(13) = 33.1, and p = 6.14×10^{-14} when compared to the Mini Analysis
600 mean AUC value in a paired samples t-test. These differences in detection performance were further
601 corroborated by the d' measure averaged across all signal-to-noise ratio conditions (Figure 4D). A
602 paired samples t-test comparing mean d' values from 'minis' (2.45 ± 0.045) versus Mini Analysis
603 (2.11 ± 0.04) gave t(13) = 14.0 and p = 3.24×10^{-9}. The same test comparing the mean d' from Mini
604 Analysis and Clampfit (1.23 ± 0.024) gave t(13) = 13.3 and p = 6.07×10^{-9}. In summary, these findings
605 clearly demonstrated that our 'minis' detection algorithm outperformed the other two algorithms,
606 for ~0.3 mV simulated minis added to real recording noise, at frequencies above 10 minis/s, while
607 Clampfit consistently showed the poorest detection performance across the entire frequency and
608 signal-to-noise range examined, for these mPSP shapes and templates.
609
610 *Detection under a wide range of frequency conditions: common errors*
611 Both 'minis' and Mini Analysis were fairly good at detecting moderately-sized (0.3 ± s.d. 0.05 mV)
612 smEPSPs added to our noise-alone recordings. Yet all three algorithms, including 'minis', missed a
613 sizeable proportion. Figure 5 shows examples of common mistakes. One type of mistake was missing
614 simulated events that occurred very close to other events (Figures 5A, B, C, D, E, F, and G).
615 Unsurprisingly, none of the three algorithms could deal with events that overlapped nearly perfectly,
616 always lumping them together. Detecting peaks in the data using thresholds or fitting templates to
617 the data cannot offer a way of identifying overlaps. Another common error type was missing events
618 with peaks on the rising phase of another mEPSP (Figures 5A, B, C, D, E, and F; green arrowheads).
619 Unlike perfect or near-perfect overlaps, these events had a clear but brief decay period that was
620 quickly upended by the rising phase of the next mini. Because these decays were brief, they were
621 often lumped with a subsequent mEPSP or they could not be adequately fit with a template by

622 Clampfit and, therefore, were discarded. The 'minis' program (but not Mini Analysis) does offer a
623 way to minimise these errors by reducing the peak integration period, but this comes at the expense
624 of noise fluctuations on the rising phase increasingly passing as postsynaptic potentials (a type of
625 false positive; Figure 5H, red arrowheads). An effective solution to this problem would, therefore,
626 require isolating and measuring the noise component in whole-cell patch clamp recordings - which
627 currently is not implemented in either Mini Analysis or Clampfit (but is in 'minis').
628
629 An even more common error type was to miss (smaller) mEPSPs that occurred on the decay phase of
630 another, often larger, earlier mEPSP (Figures 5D and G; blue arrowheads). The amplitude of mEPSPs
631 occurring on decays is effectively reduced (as the peak drops relative to the baseline, due to the
632 underlying decay of V_m) and the steeper the decay, the more the amplitude is reduced. The
633 amplitude of such a reduced mini may fall below the detection threshold and/or shape distortions
634 may prevent fitting a template. As a result, such mEPSPs were occasionally discarded (this turns out
635 to be a significant problem with real minis recorded from cortical pyramidal neurons, which exhibit
636 significant temporal summation, because of their relatively high frequencies and slow decays). There
637 is no easy way of correcting these errors, as it would (for example) require estimating the underlying
638 decaying potential and subtracting it from the overall V_m or estimating the fall in the peak and
639 adding it back to the amplitude before deciding whether to accept that candidate putative mini.
640 mEPSPs that neither occurred during the rise nor decay phases were also occasionally missed
641 (Figures 5A, D, E, and F; black arrowheads). This could have happened due to a failure to fit a
642 template (Clampfit) or due to the amplitude being reduced below threshold by *downward*
643 background noise fluctuations. In recordings of real mEPSPs, these errors would mainly affect small
644 amplitude mEPSPs. Again, an effective solution to this problem would require isolating and
645 measuring the noise component in whole-cell patch clamp recordings similarly to previously
646 discussed errors occurring on the V_m rise phase.
647

648 A whole other class of detection errors appeared in the form of false alarms (false positives)
649 occurring on the rising (Figure 5E; red arrowhead) or decaying phases (Figures 5A, B, and H; red
650 arrowheads) of underlying mEPSPs or in the absence of any other minis in the vicinity (Figures 5B
651 and H; red arrowheads). These mistakes were often caused by *upward* background noise
652 fluctuations passing as real minis and might have been 'enabled' by low amplitude detection
653 thresholds or an inability to discern shapes of real minis from mini-like noise. Just like the previously
654 discussed error type, a solution would require isolating and measuring properties of the noise
655 component. In addition, there were errors that uniquely affected only one of the algorithms, like the
656 misplacement of detected events (peaks) by Mini Analysis (Figure 5C; green arrowheads).
657
658 We saw that distinct detection errors could be made depending on how close they were to
659 neighbouring mEPSPs and whether they occurred on the rise or decay phases of other nearby
660 mEPSPs or in the absence of any other mEPSPs in the background. All three algorithms occasionally
661 committed these errors, but their incidence was uneven.
662
663 *Detection under a wide range of frequency conditions: the membrane potential 'slope trend' effect*
664 In order to quantify the detection performance in different circumstances, for the same ~0.3 mV
665 smEPSPs, we evaluated the probability of making errors in relation to the *proximity* to neighbouring
666 minis and the phase (*trend*) of the background V_m: rising or decaying. We looked at TPR as a function
667 of time interval to the nearest-neighbour mini (Figure 6A) taken together for all minis frequency
668 conditions used above (but excluding conditions where noise was scaled): i.e., 640, 320, 160, 80, 40,
669 20, 10, 5, and 2.5 minis/s conditions (9 in total). We found that detection was superior for our 'minis'
670 program across the entire inter-mini interval range. Mini Analysis came second, with Clampfit
671 consistently worst. These differences in detection performance were also reflected in the *cumulative*
672 TPR (Figure 6D). As for the FPR (Figure 6B), 'minis' was superior at detecting ~0.3 mV smEPSPs that
673 were within 10 ms of the nearest neighbour (peak-to-peak). This performance edge over Mini

674 Analysis was not maintained for larger inter-mini peak intervals, while Clampfit again showed
675 consistently the worst performance across the entire interval range. These performance differences
676 were also reflected in the *cumulative* FPR (Figure 6E). Taken together, true and false positive rates
677 allowed as to calculate a combined performance indicator, sensitivity index d', as a function of time
678 to the nearest neighbour (Figure 6C). The combined measure indicated that 'minis' had the superior
679 detection performance within 10 ms of the nearest neighbour while Clampfit showed the worst
680 performance across the entire inter-mini interval range.
681
682 During the V_m rise phase performance differences were unequivocal. There were very few events
683 and, therefore, positive detections when the background V_m was rising at 200 µV/s or faster (Figure
684 7D). Most of the detected events coinciding with the rise phase actually occurred when V_m was
685 changing at the rate of 10 to 100 µV/s. In this range 'minis' showed the best detection performance
686 with d' between 1 and 2 (Figure 7C). Mini Analysis was the second best, while Clampfit showed the
687 worst performance. This order of performance was maintained for rates below 10 µV/s with overall
688 performance improving for all algorithms. The performance edge of 'minis' over the other
689 algorithms was primarily due to low FPR (Figure 7B). The TPR of 'minis' was also superior to the
690 other two algorithms but, in terms of sensitivity, Mini Analysis was not far behind (Figure 7A). In the
691 range between 15 and 35 µV/s 'minis' actually fell slightly behind Mini Analysis. The cumulative rates
692 clearly supported the observation that 'minis' was superior to the other two algorithms with Mini
693 Analysis coming second and Clampfit having the worst performance (Figures 7D and E).
694
695 The same behaviour of the three algorithms was also observed for detecting ~0.3 mV smEPSPs
696 occurring on the decay phase of the background V_m (caused by summation of other smEPSPs). Most
697 of the detected simulated events were associated with rates of V_m change in the range of -100 and -
698 10 µV/s (Figure 8D). In this range and above, 'minis' demonstrated the best performance relative to
699 the other two algorithms with d' ranging between 1.5 and 2.5 (Figure 8C). Mini Analysis again came

700 second, while Clampfit showed very poor performance. Clampfit often had a d' that was close to 0,
701 meaning that its performance was often not different from chance level when background V_m was
702 decaying. This was mainly due to the large FPR for this algorithm (Figure 8B); 'minis' had
703 unequivocally the highest TPR and the lowest FPR (Figures 8A and B) with cumulative rates very
704 clearly reflecting this (Figures 8D and E). The overall performance of the runner-up, Mini Analysis,
705 was substantially poorer.
706
707 *Detection under realistic frequency conditions (20, 40, 80 minis/s)*
708 Data points used to construct the full virtual ROC curve include frequency and noise conditions that
709 were not necessarily realistic. Based on our calculations, the range of mEPSP frequencies one might
710 commonly expect during real recordings from neocortical pyramidal neurons is likely to be between
711 10 and 100 minis/s (see above; also G.M., unpublished experimental observations); In Figures 4A and
712 B, 20, 40 and 80 minis/s (from right to left) are highlighted by open circles. Just as across the entire
713 ROC curve, the performance of 'minis' was superior in this frequency range compared to the other
714 two algorithms with Mini Analysis coming second, and Clampfit being worst, by a substantial margin.
715
716 Other measures like true positive and false positive rates as functions of the time to the nearest
717 neighbour and V_m rate of change during the rise or decay phases pointed to a very similar conclusion
718 made regarding the full ROC curve. First, we found that 'minis' performed better than other
719 algorithms at detecting mEPSPs that were within 10 ms of other mEPSPs and that at longer delays
720 Mini Analysis performed just as well (Figure 9). Meanwhile, Clampfit performed consistently worst
721 across the range of inter-mini intervals, whether measured by d' (Figure 9C) or true positive and
722 false positive rates (Figures 9A, B, D, and E). When it came to V_m rate of change, 'minis' consistently
723 showed the best performance at detecting smEPSPs occurring with the background V_m rate of
724 change ranging between -40 and 100 µV/s (Figures 10 and 11). This is the range where the vast
725 majority of simulated events occurred (Figures 10D and 11D). In terms of individual TPR and FPR

726 (Figures 10A and B and 11A and B) and cumulative rates (Figures 10D and E and 11D and E), the
727 conclusions are much the same as those made regarding the full virtual ROC curve. Namely, that
728 'minis' had the largest TPR and the smallest FPR with an exception being the TPR in relation to rising
729 background (simulated) membrane potential trends (Figures 10A and D), with there being a range
730 (45-100 µV/s) where Mini Analysis had a slightly higher TPR, but not overall performance measured
731 as d' (Figure 10C). Similar to conditions used to construct the full ROC curve, Clampfit showed
732 consistently the worst performance by all measures. The performance of all three algorithms was
733 better with realistic smEPSP frequencies (Figures 10C and 11C) than over the full 'virtual' ROC curve
734 (Figures 7C and 8C). In summary, evaluation of detection of mEPSPs simulated at realistic
735 frequencies supported conclusions made regarding detection performance under a much broader
736 range of simulation frequencies.
737
738 **Algorithm performance comparison for detecting simulated excitatory postsynaptic potentials**
739 **with a wide set of discrete amplitudes, at realistic frequencies**
740 So far, we have only tested performance of the three algorithms when detecting moderately-sized
741 (0.3 mV ± s.d. 0.05 mV) mEPSPs with a relatively narrow range of amplitudes. The existing evidence
742 does not indicate that either mPSPs or mPSCs form a distinct amplitude distribution that can be
743 separated from the amplitude distribution of noise fluctuations. Therefore, here we aimed to test
744 the performance of detecting smEPSPs of a wide range of amplitudes, to evaluate the three
745 algorithms in more realistic settings.
746
747 We used three frequency conditions: 13, 33, and 53 minis/s. Within each of these conditions
748 smEPSPs were drawn pseudo-randomly from a uniform distribution of the following twelve discrete
749 amplitudes: 0.05, 0.1, 0.15, 0.2, 0.25, 0.3, 0.35, 0.4, 0.45, 0.5, 0.55, and 0.6 mV (4 different
750 simulations per noise trace per frequency conditions; see Methods for shapes). Just like in previous
751 simulations, we positioned these smEPSPs pseudo-randomly over noise recordings and detected

752 them using the three algorithms. The overall performance of these algorithms is shown in terms of
753 true and false positive rates in Figure 12A and d' in Figure 12B. A few things are prominent in these
754 graphs. First of all, the detection performance of all algorithms was considerably worse than when
755 detecting moderately-sized (~0.3 mV) mEPSPs. Secondly, 'minis' again had the edge over two other
756 algorithms, especially at higher mini frequencies. Third, Clampfit's performance was consistently the
757 poorest, in our hands.
758
759 Performance was also assessed pooling the frequency conditions. We found 'minis' to have the best
760 performance with the mean AUC value of 0.827 ± 0.003 (95% confidence interval from here on;
761 Figure 12C). A paired samples t-test comparing to Mini Analysis with the mean AUC value of 0.809 ±
762 0.003 gave $p = 1.0\times10^{-6}$. Clampfit showed the poorest performance, with the mean AUC value of
763 0.665 ± 0.004, $p = 2.2\times10^{-10}$ when compared to the Mini Analysis mean AUC value in a paired
764 samples t-test. These differences in detection performance were further corroborated by the d'
765 measure averaged across all frequency conditions (Figure 12D). The d' discriminability index scores
766 of 'minis' (1.5 ± 0.05) and Mini Analysis (1.33 ± 0.04) were significantly different ($p < 10^{-5}$), as were
767 the d' from Mini Analysis and Clampfit (0.61 ± 0.02) ($p < 4\times10^{-6}$) The conclusion based on combined
768 measures was in line with the assessment based on Individual frequency conditions.
769
770 Other measures like true positive and false positive rates as functions of the interval to the nearest
771 neighbour and V_m rate of change during the rise or decay phases using more realistic settings
772 pointed to a very similar conclusion to that made with the full virtual ROC curve. First, we found that
773 'minis' performed better than the other algorithms at detecting mEPSPs that were within 10 ms of
774 other mEPSPs, and that at larger intervals, Mini Analysis performed just as well (Figure 13).
775 Meanwhile, Clampfit performed consistently the worst across the range of inter-mini intervals
776 whether in terms of d' (Figure 13C) or true and false positive rates (Figures 13A, B, D, and E). When it
777 came to V_m rate of change, 'minis' performed better than Mini Analysis, which in turn performed

778 better than Clampfit when detecting smEPSPs occurring during rise and decay phases of background
779 simulated V_m (Figures 14 and 15). One difference compared to the full virtual ROC curve analysis was
780 that the detection performance of 'minis' and Mini Analysis overlapped in the range of 15-25 µV/s
781 when detecting smEPSPs occurring on the rise phase of the background V_m (Figure 14C). This is
782 largely caused by an increased FPR of 'minis' in this rate range (Figure 14B). The overall performance
783 of all algorithms was better (Figures 14C and 15C) compared to the full virtual ROC curve analysis
784 (Figures 7C and 8C), but still worse when compared to detecting moderately-sized (~0.3 mV)
785 smEPSPs with realistic frequencies (Figures 10C and 11C), as described in the previous subsection. In
786 summary, 'minis' had a substantial advantage when detecting minis in close proximity to
787 neighbouring minis, as well as during rising or falling background V_m, with Clampfit severely
788 underperforming.

Discussion

Our analysis suggests that 'mini' (mEPSC/P) frequencies typically reported in neocortical slices in the CNS synaptic function literature may be underestimated, by up to an order of magnitude. Minis are missed in part because of voltage clamp errors – a combination of space clamp errors and failures to adequately compensate series resistance – allowing charge to escape from the voltage clamp and spread to other parts of the dendritic and axonal trees, and the resulting amplitude attenuation due to filtering by the resistive and capacitive properties of dendritic membranes (Rall and Segev, 1985; Major, 1993; Spruston et al., 1993; Stuart and Spruston, 1998; Williams and Stuart, 2002; Nevian et al., 2007; Williams and Mitchell, 2008). This and other evidence (overlapping noise and minis histograms, many dendritically-detected minis being undetectable at the soma, Nevian et al. 2007) indicates there is no objective cut-off between the amplitude distributions of real mEPSP/Cs and noise fluctuations from other sources. Although using voltage recording (current clamp) addresses voltage clamp errors, the amplitude of mPSPs is also attenuated by dendritic trees (Williams and Stuart, 2002; Nevian et al., 2007; Larkum et al., 2009) as charge spreads away from the input site (synapse). These observations are a serious problem for the standard approach of using direct amplitude measurements of somatic mPSPs or mPSCs, by themselves, as an estimate of quantal size distributions in the CNS. The method essentially becomes a 'beauty contest', as arbitrary decisions have to be made about what is noise and what is a real mini, further confounded by the issue of a substantial fraction of missed minis.

The same method could, however, be used to objectively measure the properties of pure noise fluctuations (with minis blocked). This would allow one, in principle, to separate 'signal' (minis) from noise components in traces of minis recorded in the presence of noise. As the first step, we developed an effective mPSP/C detection algorithm, called 'minis'. We quantified the performance of 'minis' using standard measures from signal detection theory – namely, ROC (receiver operating

814 characteristic) curves and sensitivity index d', alongside measures of sensitivity – true positive rate
815 (TPR) and false positive rate (FPR = 1 – specificity) – and demonstrated superior performance of our
816 algorithm relative to the other two most popular algorithms in the field of minis research: Mini
817 Analysis and Clampfit. Our algorithm had a performance edge over the other two algorithms not
818 only for detecting moderately-sized (~0.3 mV) mEPSPs, but also across a wide range of realistic
819 mEPSP amplitudes, shapes and frequencies. Crucially, the latter included the higher mini frequencies
820 observed in neocortical slice experiments at body temperature, 13-80 minis/s, where temporal
821 summation becomes an increasing challenge for detection. As a necessary step in building a reliable
822 quantal size estimation method, we succeeded in developing an algorithm for detecting postsynaptic
823 events that is transparent, systematically evaluated, and flexible.
824
825 Notwithstanding its good performance, the 'minis' algorithm has important limitations. First, the
826 'minis' algorithm, just like the other two detection algorithms, cannot by itself alone be used to
827 estimate quantal sizes. Due to amplitude attenuation of spontaneous postsynaptic events and the
828 need to use amplitude detection thresholds, the estimated amplitude will generally only be an upper
829 limit on the actual population mean amplitude. We have also demonstrated that mini detection is
830 impaired on rising and decaying trends of V_m. The severity of this problem worsens with the rate of
831 change of V_m. The problem is exacerbated as the time between neighbouring minis gets shorter.
832 Therefore, the mean amplitude estimate is not only affected by the presence of noise and by
833 amplitude attenuation, but also by the presence of other miniature postsynaptic events. All the
834 above limitations also apply to estimating the frequency of postsynaptic events. All the mentioned
835 factors reduce event detectability and, therefore, result in an underestimated frequency. However,
836 'detecting' noise events as false minis can cause errors in the other direction if too low a detection
837 threshold is set. Despite these limitations, our program 'minis' fares better on this front compared to
838 the other two algorithms: 'minis' performance is also superior on rising and decaying trends in V_m,

and for closely-spaced events. To our knowledge, this is the first time these problems have been addressed, and their impact quantified in a systematic manner, and their implications discussed.

Other caveats concern the method for assessing the performance of detection algorithms. We did not use the full plausible range of realistic distributions for simulating mEPSPs in terms of their frequencies, amplitudes, and their rise and decay times. However, the shapes of these distributions are not entirely known, and this is an empirical question that remains unanswered. Because of this reason, we refrained for trying to address this question here and avoided making empirically dubious assumptions. Instead, we explored a range of scenarios where simulation frequencies ranged from more to less realistic. We explored the effects of varying signal/noise ratios. We believe that the large size of the parameter space we have explored does allow us to conclude that the three algorithms differ systematically in their performance, with our algorithm – 'minis' – being superior to the other two (in our hands at least).

We have not constructed ROC curves in the usual fashion by varying a detection threshold of each algorithm. Unfortunately, we were limited by the nature of the algorithms, specifically Clampfit which does not use a pure amplitude detection threshold but uses convolution of the data trace with each of the templates. However, our manipulations of varying the frequency of simulated events, as well as varying the amplitude of noise, allowed us to mimic effects of varying the detection threshold. We are also aware of one particular issue regarding the classification of correct rejections (true negatives). One could argue that a proper definition of correct rejections would require treating every data sample point as a potential noise event that could either be falsely detected as a signal event or correctly rejected as a noise event. Unfortunately, such a definition would result in large numbers of correct rejections (true negatives) swamping the number of other detection measures (true positives, false alarms (false positives), and misses (false negatives)) and, therefore, would make the detection performance analysis essentially meaningless. Alternatively, treating

every 10 ms noise window as a basis for correct rejection would still produce a relatively large number of correct rejections, as would similar, more complicated schemes. There is also no reason why a single noise event should be limited to a single 10 ms window. Therefore, we thought that a reasonably practical definition of correct rejections as rejected prominent noise fluctuations fared better than the alternatives. Having explicit, transparent, and reproducible, methods to benchmark the performance is better than relying on subjective examination of recording traces.

Finally, we would like to address the question of whether we used optimal detection settings for each algorithm. Mini Analysis settings were similar to those of 'minis'. The two algorithms are somewhat similar and chosen settings were observed to give the best performance for both algorithms when detecting simulated mPSPs, after considerable exploration. In case there is any doubt about our method, we have made our recorded and simulated data and Matlab analysis code publicly available. With regards to using Clampfit to analyse simulated data, we used 9 templates (the maximum allowed) constructed in a typical fashion by averaging a number of waveforms with similar shapes but separating qualitatively different shapes. These templates have also been made available publicly. We tested different detection regimes with templates based on both smoothed or unsmoothed traces and comparing detection of smoothed and unsmoothed recording traces and chose the best regime. However, we did not construct new templates for every new recording or every new simulation condition, because this is extremely time-consuming and is not an efficient way to conduct this type of analysis, although Clampfit detection performance might have improved marginally. Clampfit might perform better if the number of templates was not limited to 9, and if a wide range of inbuilt templates was available. These issues are, however, outside the scope of this study. Given these considerations, we are confident in the validity of our approach.

In the discussion of errors made by different detection algorithms, we alluded to the usefulness of being able to estimate properties of V_m noise fluctuations. Noise events could potentially be

‘removed’ from the combined signal and noise event distribution by direct histogram subtraction, although in practice it turns out one needs to compensate for the decay of the underlying waveform, following minis (MD & GM, unpublished observations). Alternatively, noise traces can be used to more accurately ‘reverse-engineer’ the signal distribution via simulations, by iteratively adjusting the shapes, amplitudes, and frequencies of simulated minis, and adding these to real noise, under the control of an optimisation algorithm to match up the distributions of *simulated* minis plus real noise to *real* minis plus real noise. A future paper will explore this and present a quantal analysis method based on the ‘minis’ spontaneous postsynaptic event detection algorithm.

References

Bekkers JM (1994) Quantal analysis of synaptic transmission in the central nervous system. Curr Opin Neurobiol 4:360–365.

Biró ÁA, Holderith NB, Nusser Z (2005) Quantal Size Is Independent of the Release Probability at Hippocampal Excitatory Synapses. The Journal of Neuroscience 25:223–232.

Brown TH, Wong RKS, Prince DA (1979) Spontaneous miniature synaptic potentials in hippocampal neurons. Brain Res 177:194–199.

Clamann HP, Rioult-Pedotti MS, Luscher HR (1991) The influence of noise on quantal EPSP size obtained by deconvolution in spinal motoneurons in the cat. J Neurophysiol 65:67–75.

Clements JD (2003) Variance–mean analysis: a simple and reliable approach for investigating synaptic transmission and modulation. J Neurosci Methods 130:115–125.

Clements JD, Silver RA (2000) Unveiling synaptic plasticity: a new graphical and analytical approach. Trends Neurosci 23:105–113.

del Castillo J, Katz B (1954) Quantal components of the end-plate potential. J Physiol 124:560–573.

Dervinis M (2023a) Intracellular membrane potential noise recordings and mEPSP simulations in cortical pyramidal cells used to benchmark “minis” software. G-Node. https://doi.org/10.12751/g-node.inpx5x.

Dervinis M (2023b) dervinism/minis-benchmarking. Zenodo. https://doi.org/10.5281/zenodo.8336130.

Dervinis M (2023c) dervinism/minis. Zenodo. https://doi.org/10.5281/zenodo.8336025.

Edwards FR, Redman SJ, Walmsley B (1976) Statistical fluctuations in charge transfer at Ia synapses on spinal motoneurones. J Physiol 259:665–688.

Enoki R, Hu Y, Hamilton D, Fine A (2009) Expression of Long-Term Plasticity at Individual Synapses in Hippocampus Is Graded, Bidirectional, and Mainly Presynaptic: Optical Quantal Analysis. Neuron 62:242–253.

Eyal G, Verhoog MB, Testa-Silva G, Deitcher Y, Benavides-Piccione R, DeFelipe J, de Kock CPJ, Mansvelder HD, Segev I (2018) Human Cortical Pyramidal Neurons: From Spines to Spikes via Models. Front Cell Neurosci 12:1–24.

Fatt P, Katz B (1952) Spontaneous subthreshold activity at motor nerve endings. J Physiol 117:109–128.

Forti L, Bossi M, Bergamaschi A, Villa A, Malgaroli A (1997) Loose-patch recordings of single quanta at individual hippocampal synapses. Nature 388:874–878.

Hardingham NR, Read JCA, Trevelyan AJ, Nelson JC, Jack JJB, Bannister NJ (2010) Quantal Analysis Reveals a Functional Correlation between Presynaptic and Postsynaptic Efficacy in Excitatory Connections from Rat Neocortex. The Journal of Neuroscience 30:1441–1451.

934 Heuser JE, Reese TS, Dennis MJ, Jan Y, Jan L, Evans L (1979) Synaptic vesicle exocytosis captured by
935 quick freezing and correlated with quantal transmitter release. Journal of Cell Biology 81:275–
936 300.

937 Holler S, Köstinger G, Martin KAC, Schuhknecht GFP, Stratford KJ (2021) Structure and function of a
938 neocortical synapse. Nature 591:111–116.

939 Isaacson JS, Walmsley B (1995) Counting quanta: Direct measurements of transmitter release at a
940 central synapse. Neuron 15:875–884.

941 Jack JJ, Redman SJ, Wong K (1981) The components of synaptic potentials evoked in cat spinal
942 motoneurones by impulses in single group Ia afferents. J Physiol 321:65–96.

943 Jonas P, Major G, Sakmann B (1993) Quantal components of unitary EPSCs at the mossy fibre
944 synapse on CA3 pyramidal cells of rat hippocampus. J Physiol 472:615–663.

945 Katz B (1969) The Release of Neural Transmitter Substances. Liverpool: Liverpool Univ. Press.

946 Korn H, Faber DS (1991) Quantal analysis and synaptic efficacy in the CNS. Trends Neurosci 14:439–
947 445.

948 Kraszewski K, Grantyn R (1992) Unitary, quantal and miniature gaba-activated synaptic chloride
949 currents in cultured neurons from the rat superior colliculus. Neuroscience 47:555–570.

950 Kullmann DM, Nicoll RA (1992) Long-term potentiation is associated with increases in quantal
951 content and quantal amplitude. Nature 357:240–244.

952 Kuno M (1964) Quantal components of excitatory synaptic potentials in spinal motoneurones. J
953 Physiol 175:81–99.

954 Larkman A, Stratford K, Jack J (1991) Quantal analysis of excitatory synaptic action and depression in
955 hippocampal slices. Nature 350:344–347.

956 Larkman AU (1991) Dendritic morphology of pyramidal neurones of the visual cortex of the rat: III.
957 Spine distributions. Journal of Comparative Neurology 306:332–343.

958 Larkum ME, Nevian T, Sandler M, Polsky A, Schiller J (2009) Synaptic Integration in Tuft Dendrites of
959 Layer 5 Pyramidal Neurons: A New Unifying Principle. Science (1979) 325:756–760.

960 Liu Z et al. (2022) Sustained deep-tissue voltage recording using a fast indicator evolved for two-
961 photon microscopy. Cell 185:3408-3425.e29.

962 Macmillan NA, Creelman CD (2005) Detection theory: A user's guide, 2nd ed. Mahwah, NJ, US:
963 Lawrence Erlbaum Associates Publishers.

964 Major G (1993) Solutions for transients in arbitrarily branching cables: III. Voltage clamp problems.
965 Biophys J 65:469–491.

966 Major G, Evans JD, Jack JJ (1993) Solutions for transients in arbitrarily branching cables: I. Voltage
967 recording with a somatic shunt. Biophys J 65:423–449.

968 Major G, Larkum ME, Schiller J (2013) Active Properties of Neocortical Pyramidal Neuron Dendrites.
969 Annu Rev Neurosci 36:1–24.

Motta A, Berning M, Boergens KM, Staffler B, Beining M, Loomba S, Hennig P, Wissler H, Helmstaedter M (2019) Dense connectomic reconstruction in layer 4 of the somatosensory cortex. Science (1979) 366:eaay3134.

Murthy VN, Stevens CF (1999) Reversal of synaptic vesicle docking at central synapses. Nat Neurosci 2:503–507.

Nevian T, Larkum ME, Polsky A, Schiller J (2007) Properties of basal dendrites of layer 5 pyramidal neurons: a direct patch-clamp recording study. Nat Neurosci 10:206–214.

Oertner TG, Sabatini BL, Nimchinsky EA, Svoboda K (2002) Facilitation at single synapses probed with optical quantal analysis. Nat Neurosci 5:657–664.

Peled ES, Isacoff EY (2011) Optical quantal analysis of synaptic transmission in wild-type and rab3-mutant Drosophila motor axons. Nat Neurosci 14:519–526.

Rall W (1977) Core Conductor Theory and Cable Properties of Neurons. In: Handbook of physiology, cellular biology of neurons (Kandel ER, Brookhardt JM, Mountcastle VM, eds), pp 39–97. Bethesda, MD: American Physiological Society.

Rall W, Segev I (1985) Space-clamp problems when voltage clamping branched neurons with intracellular microelectrodes. In: Voltage and Patch Clamping with Microelectrodes (T. G. Smith Jr, Lecar H, Redman SJ, Gage P, eds), pp 191–215. Bethesda, MD: American Physiological Society.

Redman S (1990) Quantal analysis of synaptic potentials in neurons of the central nervous system. Physiol Rev 70:165–198.

Reid CA, Clements JD (1999) Postsynaptic expression of long-term potentiation in the rat dentate gyrus demonstrated by variance-mean analysis. J Physiol 518:121–130.

Sahara Y, Takahashi T (2001) Quantal components of the excitatory postsynaptic currents at a rat central auditory synapse. J Physiol 536:189–197.

Silver RA (2003) Estimation of nonuniform quantal parameters with multiple-probability fluctuation analysis: theory, application and limitations. J Neurosci Methods 130:127–141.

Spruston N, Jaffe DB, Williams SH, Johnston D (1993) Voltage- and space-clamp errors associated with the measurement of electrotonically remote synaptic events. J Neurophysiol 70:781–802.

Stern P, Edwards FA, Sakmann B (1992) Fast and slow components of unitary EPSCs on stellate cells elicited by focal stimulation in slices of rat visual cortex. J Physiol 449:247–278.

Stuart G, Spruston N (1998) Determinants of Voltage Attenuation in Neocortical Pyramidal Neuron Dendrites. The Journal of Neuroscience 18:3501–3510.

Vere-Jones D (1966) SIMPLE STOCHASTIC MODELS FOR THE RELEASE OF QUANTA OF TRANSMITTER FROM A NERVE TERMINAL. Australian Journal of Statistics 8:53–63.

Wall MJ, Usowicz MM (1998) Development of the quantal properties of evoked and spontaneous synaptic currents at a brain synapse. Nat Neurosci 1:675–682.

Williams SR, Mitchell SJ (2008) Direct measurement of somatic voltage clamp errors in central neurons. Nat Neurosci 11:790–798.

1008 Williams SR, Stuart GJ (2002) Dependence of EPSP Efficacy on Synapse Location in Neocortical
1009 Pyramidal Neurons. Science (1979) 295:1907–1910.

1010 Yuste R, Majewska A, Cash SS, Denk W (1999) Mechanisms of Calcium Influx into Hippocampal
1011 Spines: Heterogeneity among Spines, Coincidence Detection by NMDA Receptors, and Optical
1012 Quantal Analysis. The Journal of Neuroscience 19:1976–1987.

1013

1014

Figures

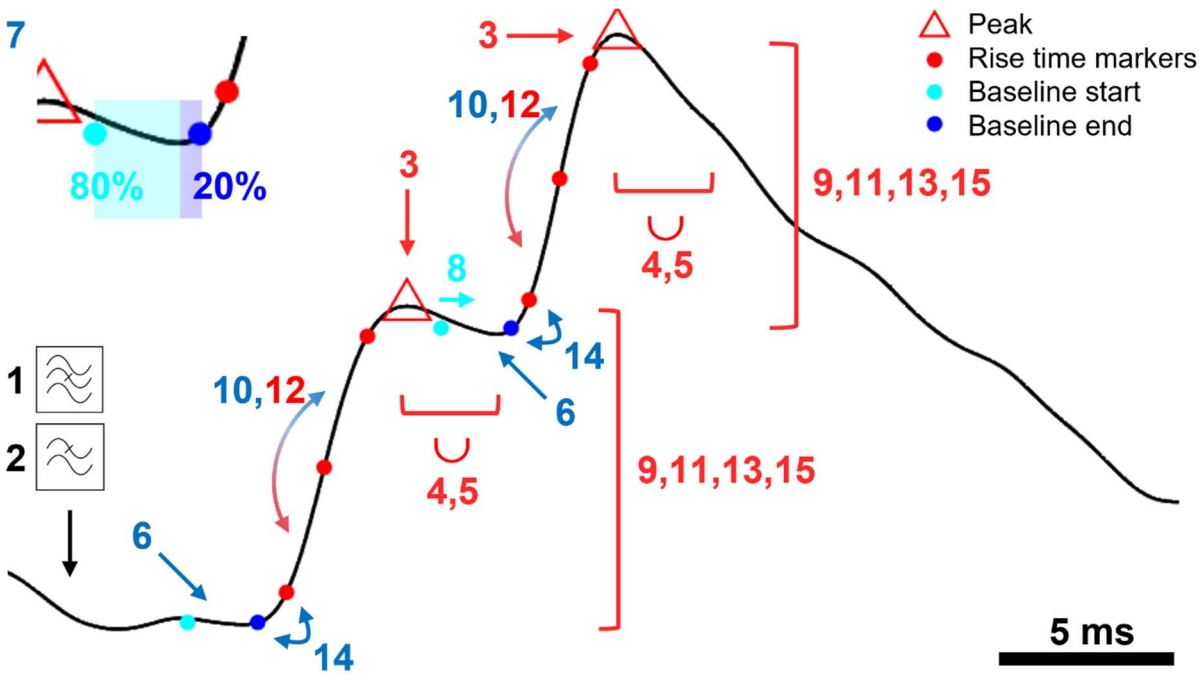

Figure 1: A Schematic representation of key steps in 'minis' detection algorithm.

An illustration of a step-by-step application of the mPSP/C detection algorithm using simulated data. Numbered steps dealing with mini peaks/amplitudes are shown in red, steps used to determine the baseline are shown in blue. Briefly, the steps are:

1. Bandstop filter (against mains).
2. Lowpass filter to remove high frequency noise.
3. Find peaks.
4. Discard smaller peaks with the peak integration period represented by the length of the bracket and the union symbol (∪).
5. Move to a higher peak (if exists) within the peak integration period discarding the earlier peak.
6. Position the baseline at a local minimum located within the time-to-peak period prior to the peak.

7. Position the baseline asymmetrically (80:20) around the minimum (colour change at the inset).
8. Correct the start of the baseline if it overlaps with the previous peak.
9. Discard the peak if it falls outside the acceptable amplitude range (repeated three more times).
10. Compare rise time halves to correct the baseline (can be repeated once more).
11. Repeat Step 9.
12. Compare rise time halves to correct the peak.
13. Repeat Step 9.
14. Correct the baseline if it significantly deviates from the 10%/20% rise time mark.
15. Repeat Step 9.

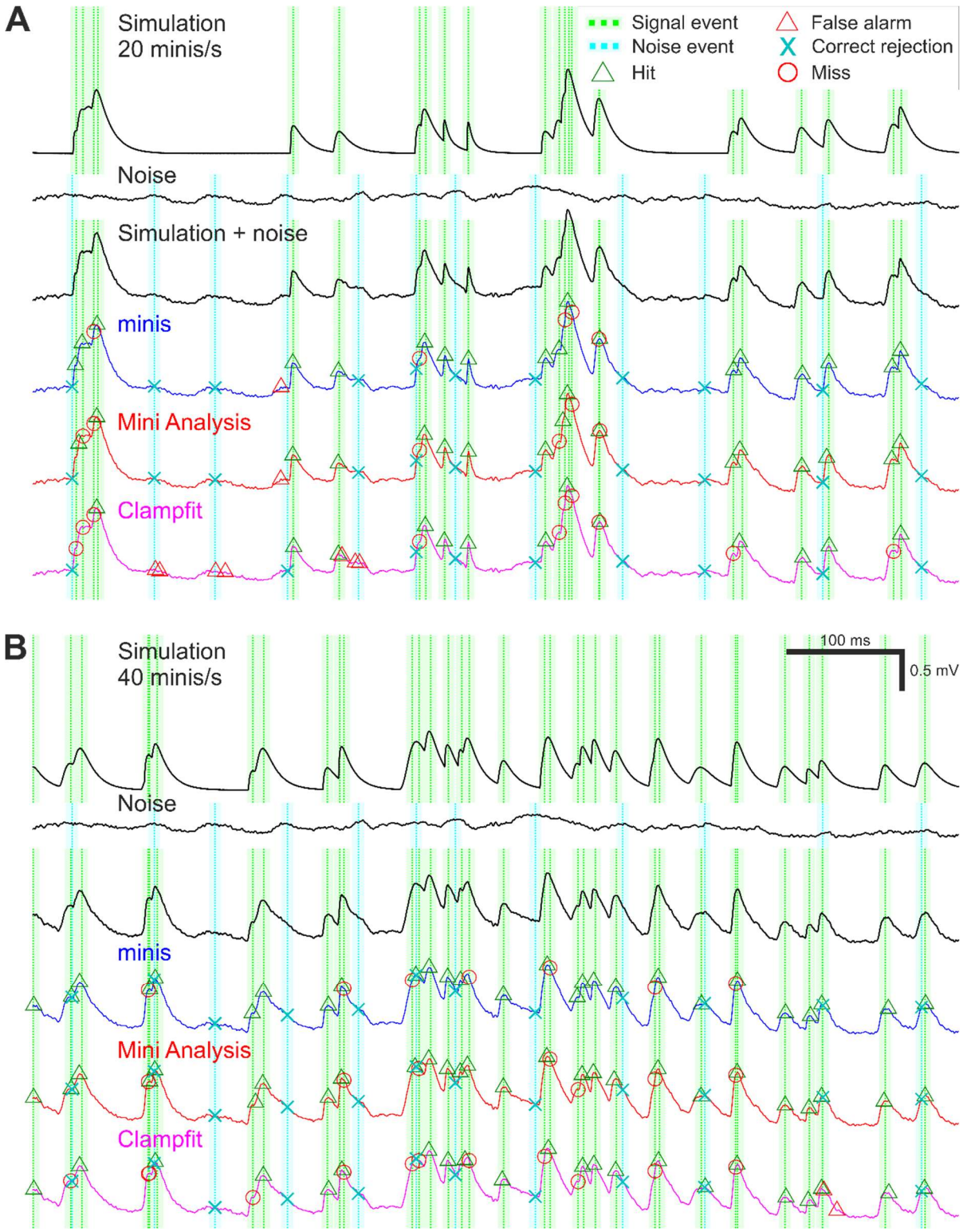

Figure 2: Simulation and detection performance.

(A) An example of simulated membrane potential recording with average simulated mEPSP frequency of 20 minis/s. The top voltage trace shows a brief segment with randomly timed smEPSPs with random, normally-distributed amplitudes (μ_1= 0.3 mV, σ_1 = 0.05 mV) and 10-90% rise times

1046 (drawn from the upper half of the distribution with μ_2 = 0.05 ms, σ_2 = 2.5 ms); see Methods. Dotted
1047 green vertical lines mark signal events corresponding to smEPSP peaks. The paler shaded colour
1048 demarcates a 10-ms (± 5 ms) window for accepting the detection of a signal event. The second
1049 traces from the top are corresponding recordings of V_m noise fluctuations (the 2nd recording phase:
1050 'noise-alone' condition, in TTX and transmitter blockers), after initial filtering and smoothing (steps 1
1051 and 2 of the 'minis' detection algorithm). Dotted vertical cyan lines indicate noise events; the shaded
1052 colour demarcates a window of exclusion for correctly rejecting these events (see Methods). The V_m
1053 third from the top trace is a hybrid one with smEPSPs added to the noise recording and with signal
1054 events and noise 'events' indicated. The coloured V_m traces below show detection performance for
1055 the three different algorithms.
1056 (B) An example of simulated V_m recording with mEPSP frequency of 40 minis/s.

1057

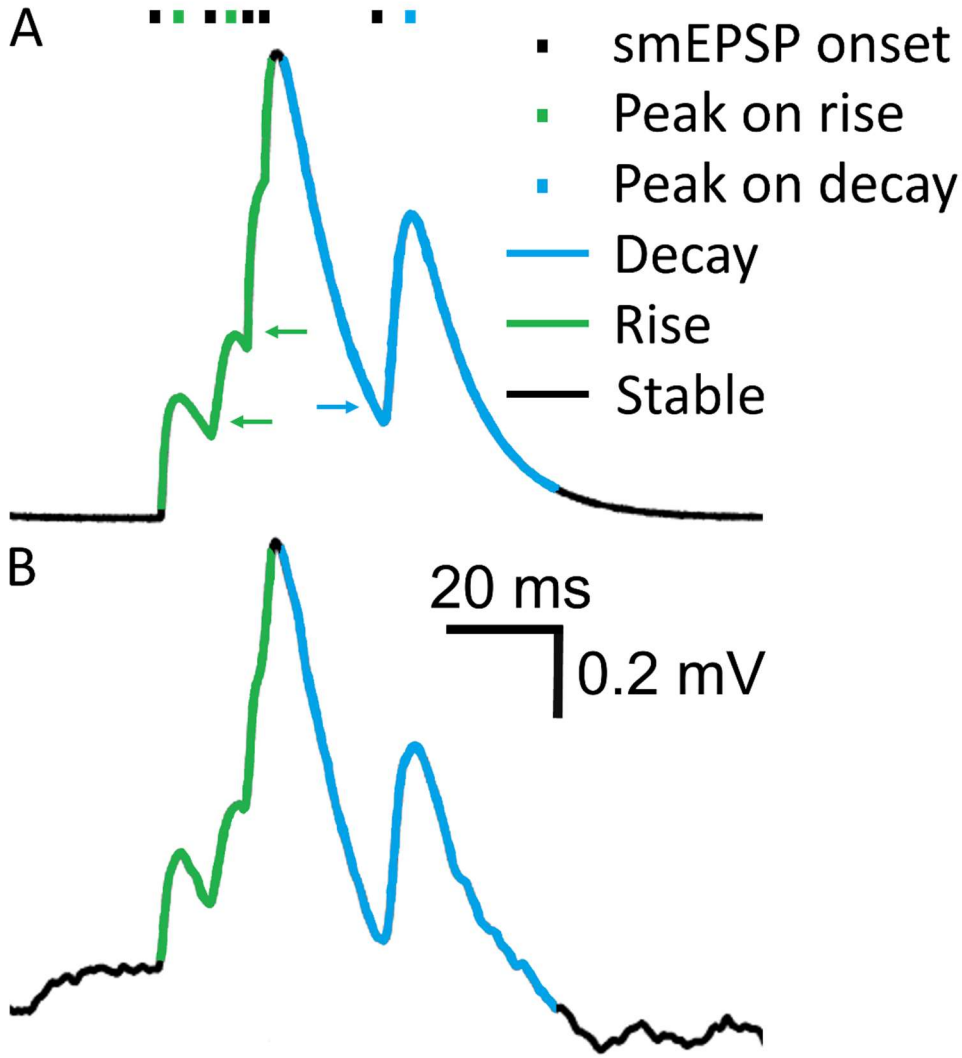

Figure 3: Membrane potential rising, steady-ish and falling 'trend phases'.

(A) A short segment of a V_m trace showing five smEPSPs. Different V_m 'trend phases', based on the overall upward or downward trend in *simulated* voltage, are marked in colour. Green arrows indicate V_m points where the V_m rate of increase is assigned to the preceding mEPSP peak. The blue arrow indicates a V_m point where the V_m rate of decay is assigned to the following mEPSP peak. (B) Simulated V_m trace in (A) added to a noise recording. V_m 'trend phases' were determined in (A) and are used to classify detected events in (B).

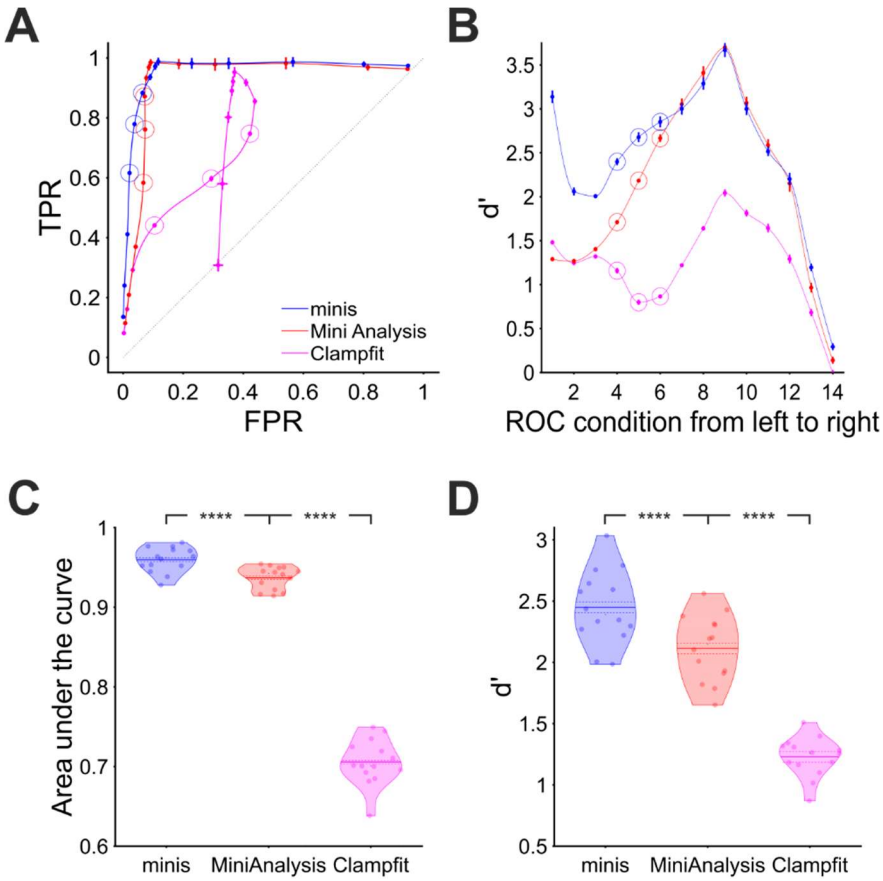

Figure 4: Overall performance for detecting 'moderately'-sized smEPSPs (~0.3 mV). (A) 'virtual' ROC (Receiver Operator Characteristic)-like curve showing performance for detecting 'moderately'-sized smEPSPs in terms of True Positive Rate TPR (sensitivity) and False Positive Rate FPR (1 – specificity) for all three algorithms, averaged across all 14 cells. In each case, dataset varies from point to point, as opposed to detection threshold itself (which is varied systematically in a traditional ROC, using one dataset). Ideal performance would be a right-angle plot going vertically up TPR-axis at FPR=0, then horizontally along the top of the plot at TPR=1; minis is close to ideal, and superior to Mini Analysis, which is not too far from ideal (despite its 'missed minis' problems). Clampfit is far from ideal. Different points represent 14 different frequency/signal-to-noise ratio conditions, averaged across all 14 cells. Moving (generally) from bottom to top/left to right, simulated minis rates and signal-to-noise ratio are decreasing. Vertical and horizontal bars indicate 95% confidence interval around each mean. The dotted diagonal line indicates chance performance. The hollow circles mark three realistic smEPSP frequencies (80, 40, and 20 minis/s).

1081 (B) Sensitivity (discriminability) index (d') in the same 14 conditions as in (A) for all three algorithms,

1082 averaged across all 14 cells.

1083 (C) 'Violin' plots for Area under the virtual-ROC curve in (A) for all three algorithms. Individual data

1084 points represent the 14 individual recordings (cells), horizontally 'swarmed' to avoid overlaps. AUC

1085 (Area Under Curve) is averaged across all 14 frequency/signal-to-noise conditions for each cell for

1086 each detection algorithm. The mean is marked by a solid line over the 'violin' centre. The dashed line

1087 indicates the 95% confidence limits of the mean, and coloured shapes indicate the approximate

1088 (smoothed) probability densities (wider = higher probability of those values).

1089 **** indicates (highly) significantly different at $p \leq 10^{-5}$ level, paired t-test.

1090 (D) Similar plot for sensitivity index d' averaged across all 14 frequency/signal-to-noise conditions for

1091 each cell and each detection algorithm.

1092

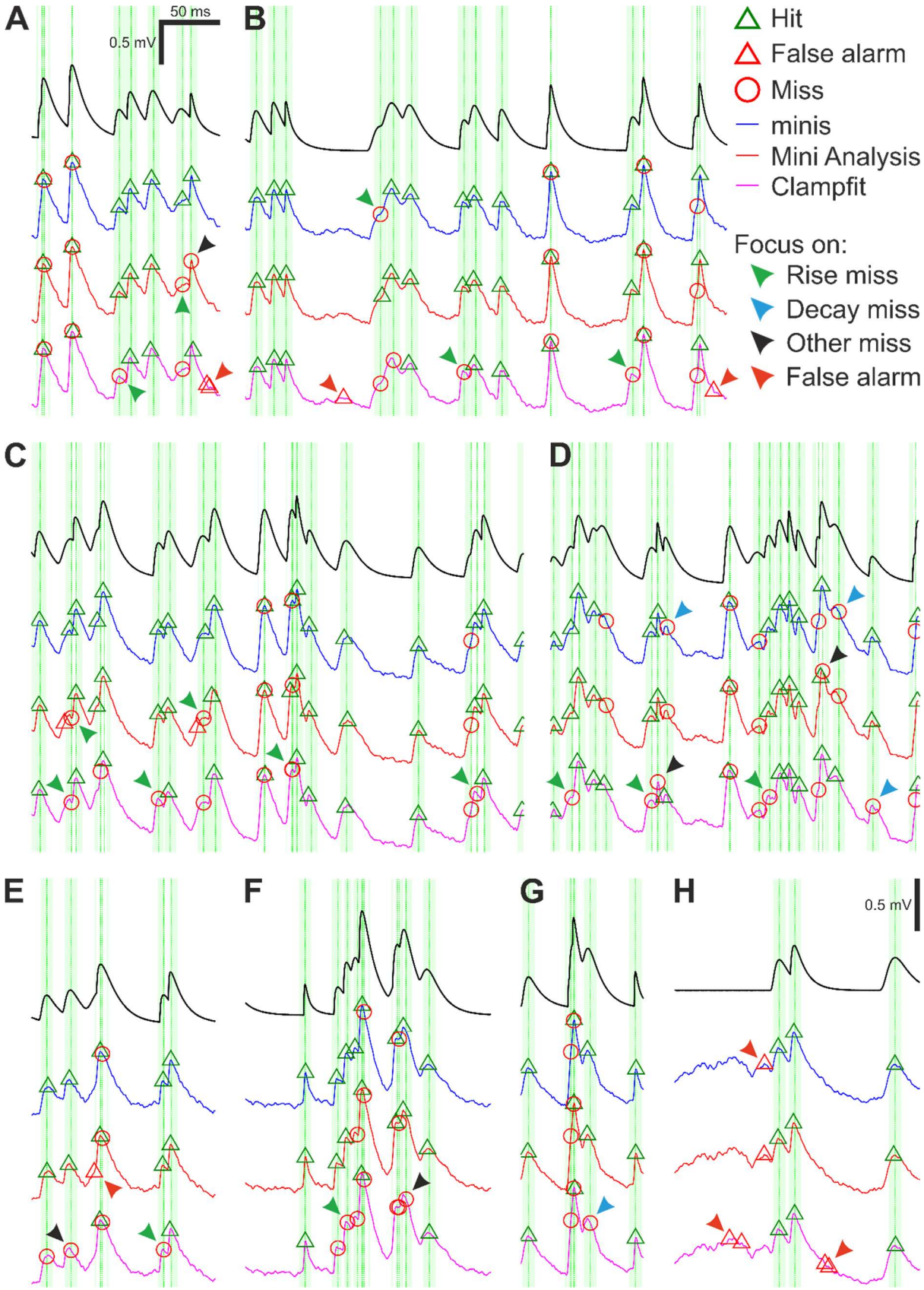

1093

1094 **Figure 5**: Moderately-sized (~0.3 mV) smEPSPs (40 minis/s): detection errors made by the three

1095 algorithms.

(A-H) Examples of smEPSP detection errors commonly committed by the three algorithms. Traces in blue, red, and magenta represent detection performance for ‘minis’, Mini Analysis, and Clampfit, respectively. The top black trace shows actual smEPSPs. Vertical green dotted lines mark actual individual (i.e., non-summated) smEPSP peak locations with the fainter shaded colour demarcating a 10-ms window for accepting the detection of an mEPSP. Arrowheads indicate common detection errors made by the three algorithms. (Details in text).

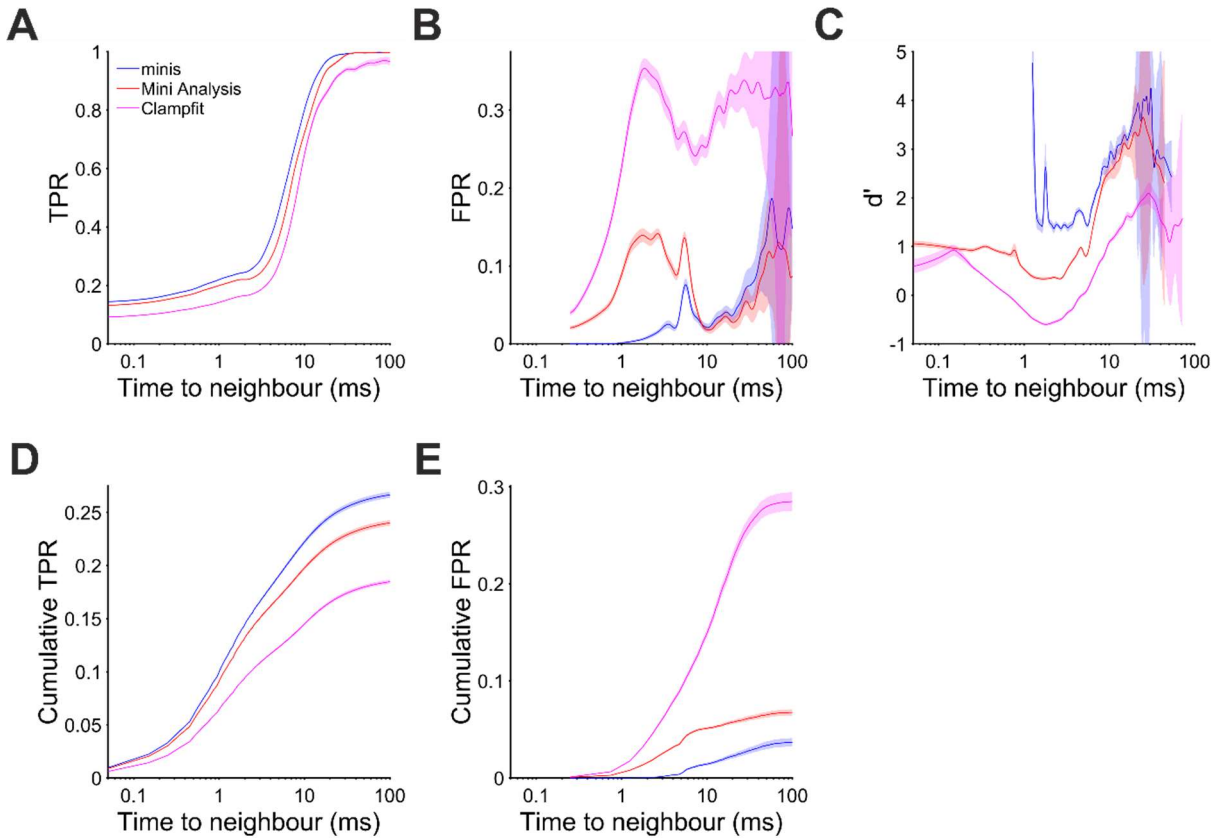

Figure 6: Performance when detecting moderately-sized (~0.3 mV) smEPSPs as a function of time to the nearest neighbour (mean inter-mini peak-to-peak interval). Pale shaded colours indicate 95% confidence intervals.

(A) True positive rate (TPR).

(B) False positive rate (FPR).

(C) Sensitivity index d' (undefined but arbitrarily high for TPR > 0 and FPR = 0, e.g. for inter-mini intervals below 1 ms, for minis algorithm).

(D) Cumulative true positive rate (TPR) (cumulative true positives normalised by the total unbanded true positive count and scaled by the overall unbanded TPR; see text for details).

(E) Cumulative FPR (cumulative false positives normalised by the total unbanded false positive count and scaled by the overall unbanded FPR).

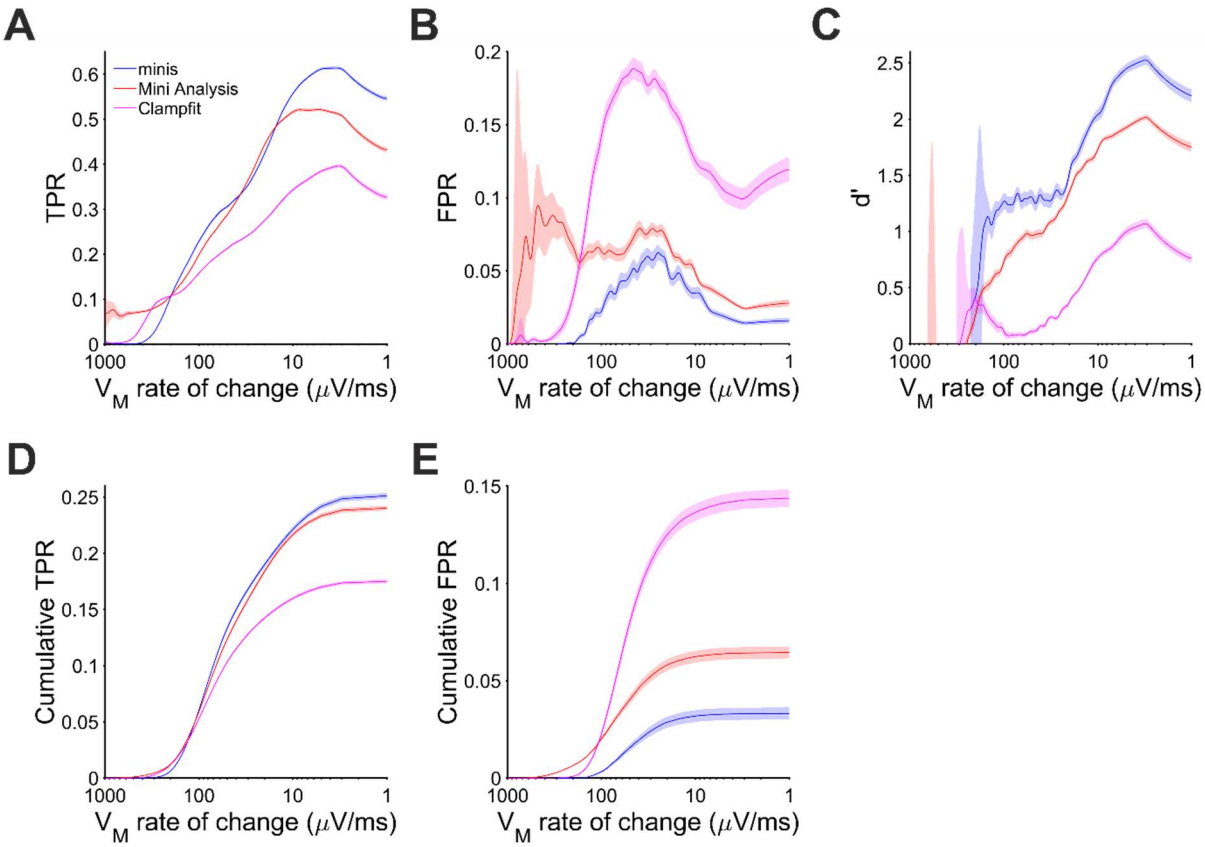

Figure 7: Performance when detecting moderately-sized (~0.3 mV) smEPSPs on a rising trend V_m as a function of the V_m rate of change. Paler shaded colours indicate 95% confidence intervals.

(A) True positive rate (TPR).

(B) False positive rate (FPR).

(C) Sensitivity index d'.

(D) Cumulative TPR.

(E) Cumulative FPR.

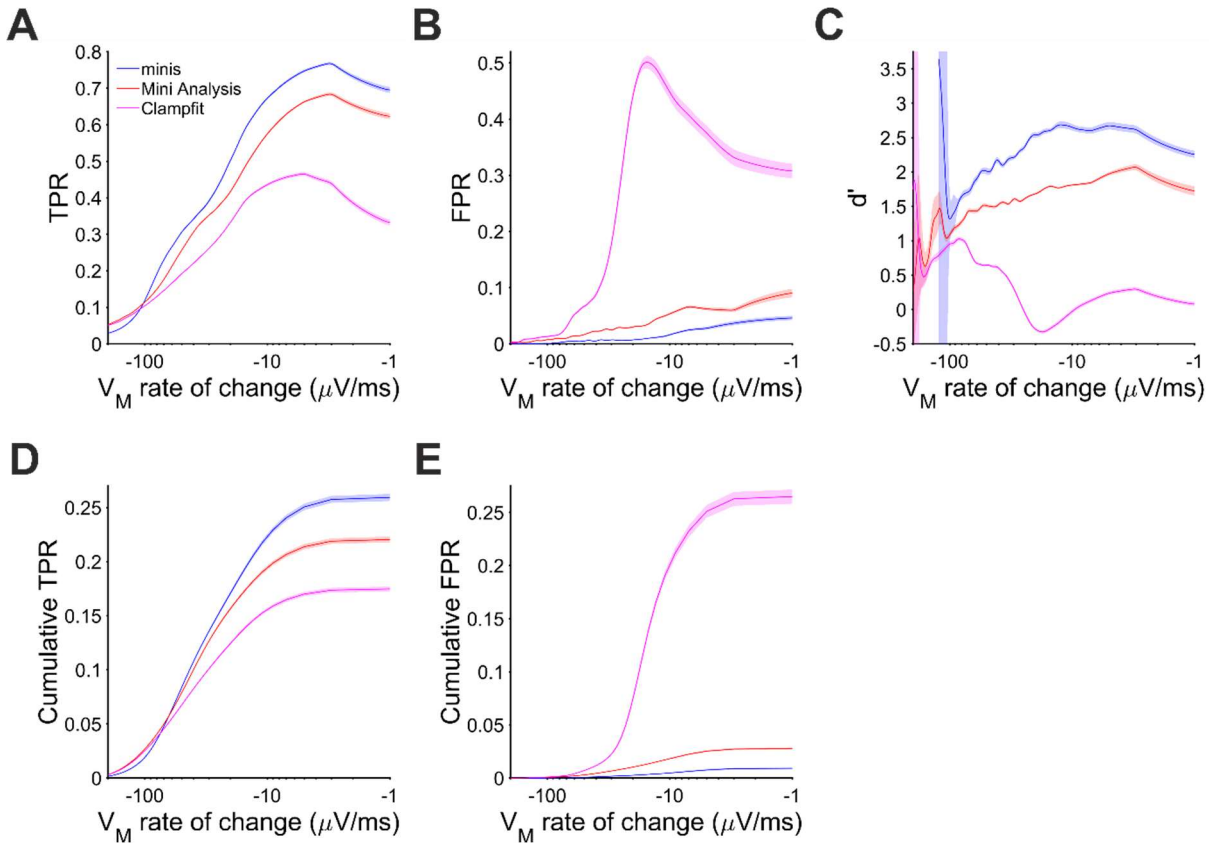

Figure 8: Performance when detecting moderately-sized (~0.3 mV) smEPSPs on the membrane potential decaying trend phase as a function of the membrane potential rate of change. Paler shaded colours indicate 95% confidence intervals.

(A) True positive rate (TPR)

(B) False positive rate (FPR).

(C) Sensitivity Index d'.

(D) Cumulative TPR.

(E) Cumulative FPR.

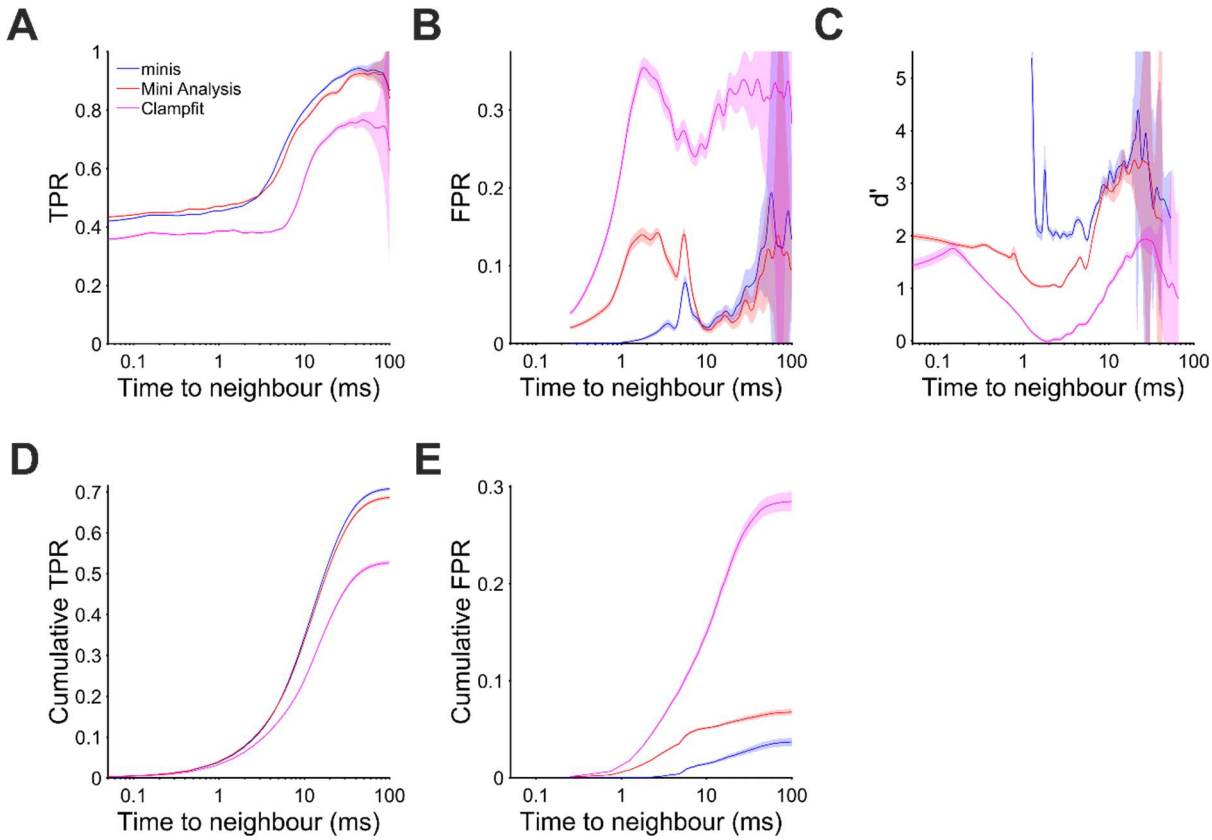

Figure 9: Performance when detecting moderately-sized (~0.3 mV) smEPSPs as a function of time to the nearest neighbour with realistic mini rates (20, 40, 80 minis/s). Paler shaded colours indicate 95% confidence intervals.

(A) True positive rate (TPR).

(B) False positive rate (FPR).

(C) Sensitivity index d' (undefined but arbitrarily high for TPR > 0 and FPR = 0, e.g. for inter-mini intervals below 1 ms, for minis algorithm).

(D) Cumulative TPR.

(E) Cumulative FPR.

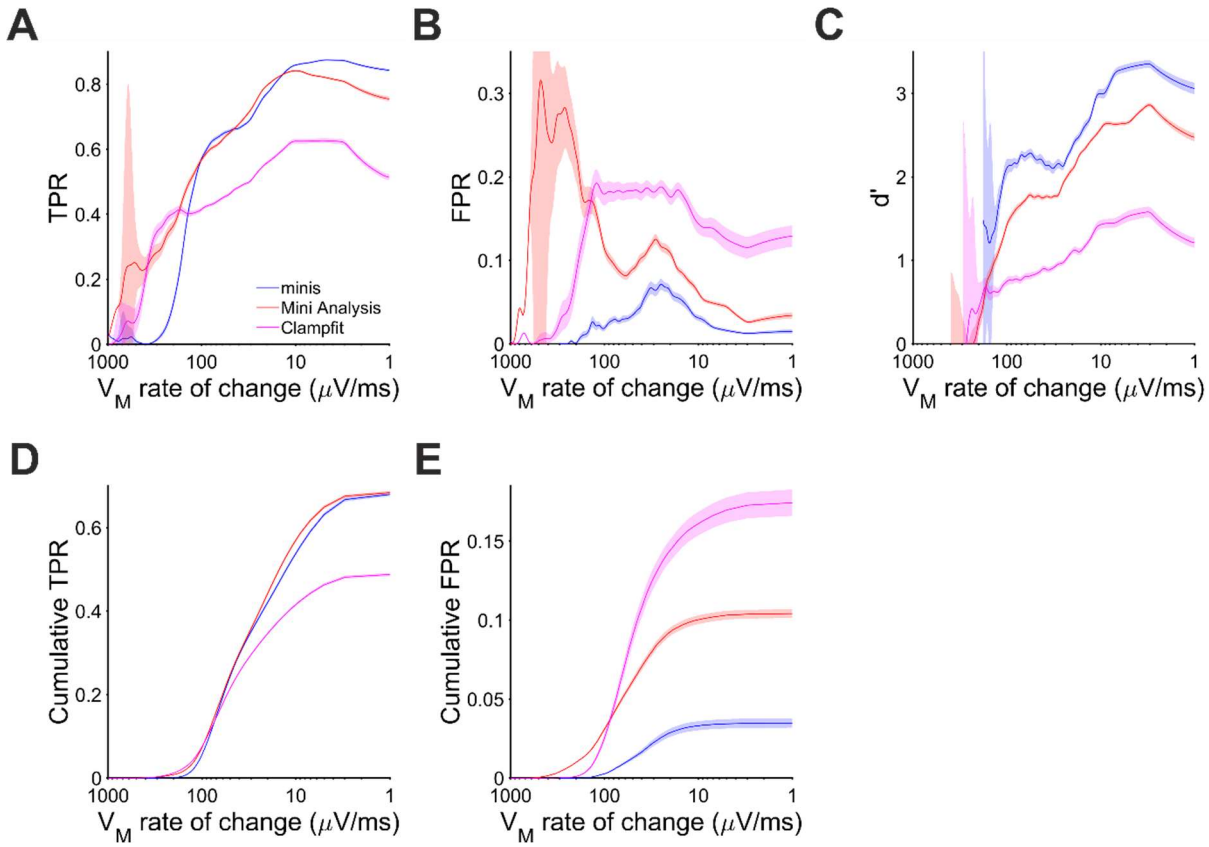

Figure 10: Performance when detecting moderately-sized (~0.3 mV) smEPSPs on the rising trend V_m phases with realistic mini rates (20, 40, 80 minis/s, as in Fig. 9), as a function of the rate of change of V_m. Pale shaded colours indicate 95% confidence intervals.

(A) True positive rate (TPR)

(B) False positive rate (FPR).

(C) Sensitivity index d'.

(D) Cumulative TPR.

(E) Cumulative FPR.

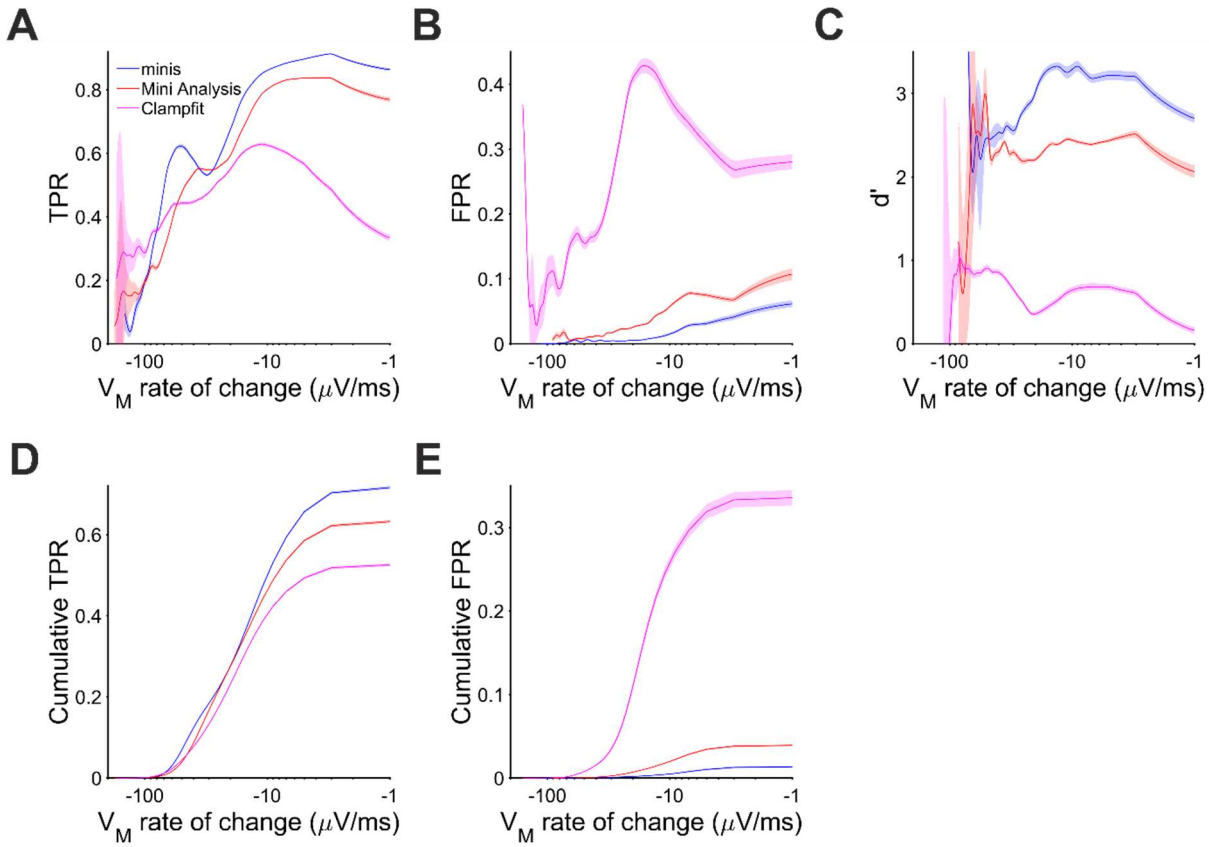

Figure 11: Performance when detecting moderately-sized (~0.3 mV) smEPSPs on the membrane potential decay phase with realistic minis rates (20, 40, 80 minis/s, as in Figs. 9 and 10). Pale shaded colours indicate 95% confidence intervals.

(A) True positive rate (TPR) when detecting moderately-sized smEPSPs on the V_m decay phase as a function of the V_m rate of change.

(B) False positive rate (FPR).

(C) Sensitivity index d'.

(D) Cumulative TPR.

(E) Cumulative FPR.

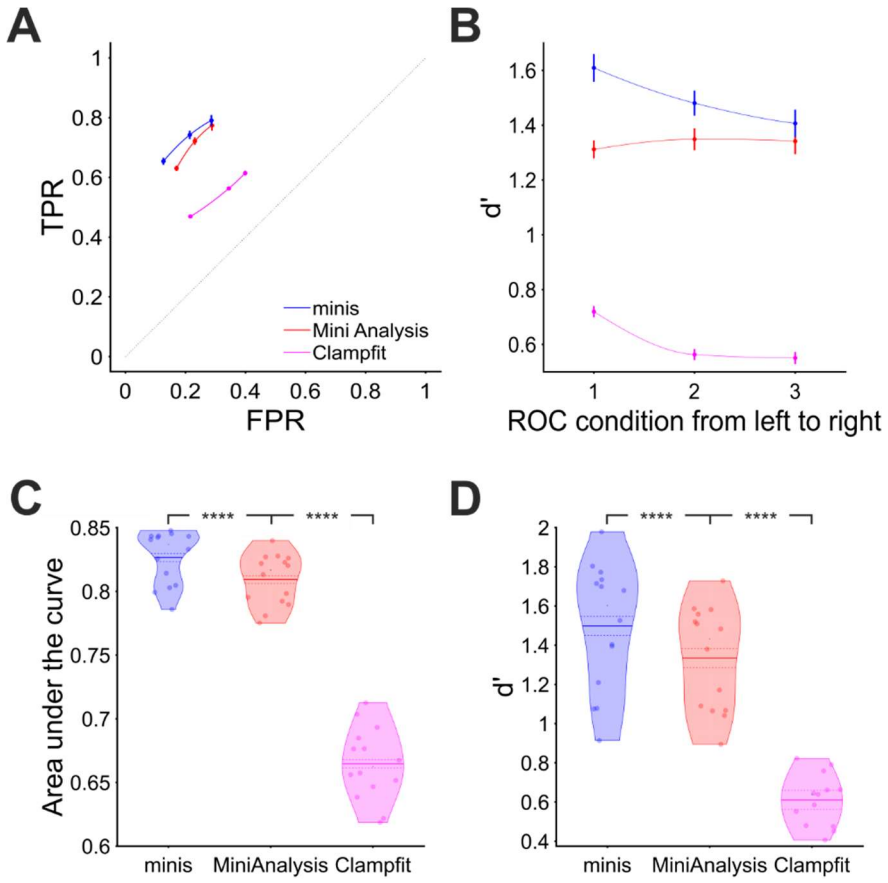

1167

1168 **Figure 12**: Overall performance for detecting smEPSPs of various (realistic) discrete amplitudes at

1169 'realistic' mini rates (details in text).

1170 (A) Partial virtual "ROC" curve showing performance for detecting small-to-large-sized smEPSPs (0.05

1171 to 0.6 mV in increments of 0.05 mV selected and added at random to a noise trace from each of the

1172 14 cells) in terms of TPR (sensitivity) and FPR (1 – specificity) for all three algorithms. Moving from

1173 left to right different data points represent 3 different biologically realistic frequency conditions: 53,

1174 33, and 13 minis/s. Vertical and horizontal bars indicate 95% confidence interval around the mean.

1175 The dotted diagonal line indicates chance performance.

1176 (B) Sensitivity index (d') when detecting smEPSPs in the same 3 conditions as in (A) for all three

1177 algorithms.

1178 (C) Area under the virtual-ROC curve in (A) for all three algorithms. Individual data points represent

1179 individual recordings (n=14 cells), averaged over the three simulated minis frequencies. The mean is

1180 marked by a solid line over the violin centre. The dashed line indicates the 95% confidence limits.

1181 **** indicates (highly) significantly different at $p \leq 10^{-5}$ level, paired t-test.

1182 (D) Sensitivity index d' averaged across all three simulated minis frequencies, for each cell (n=14),

1183 separately for each detection algorithm.

1184

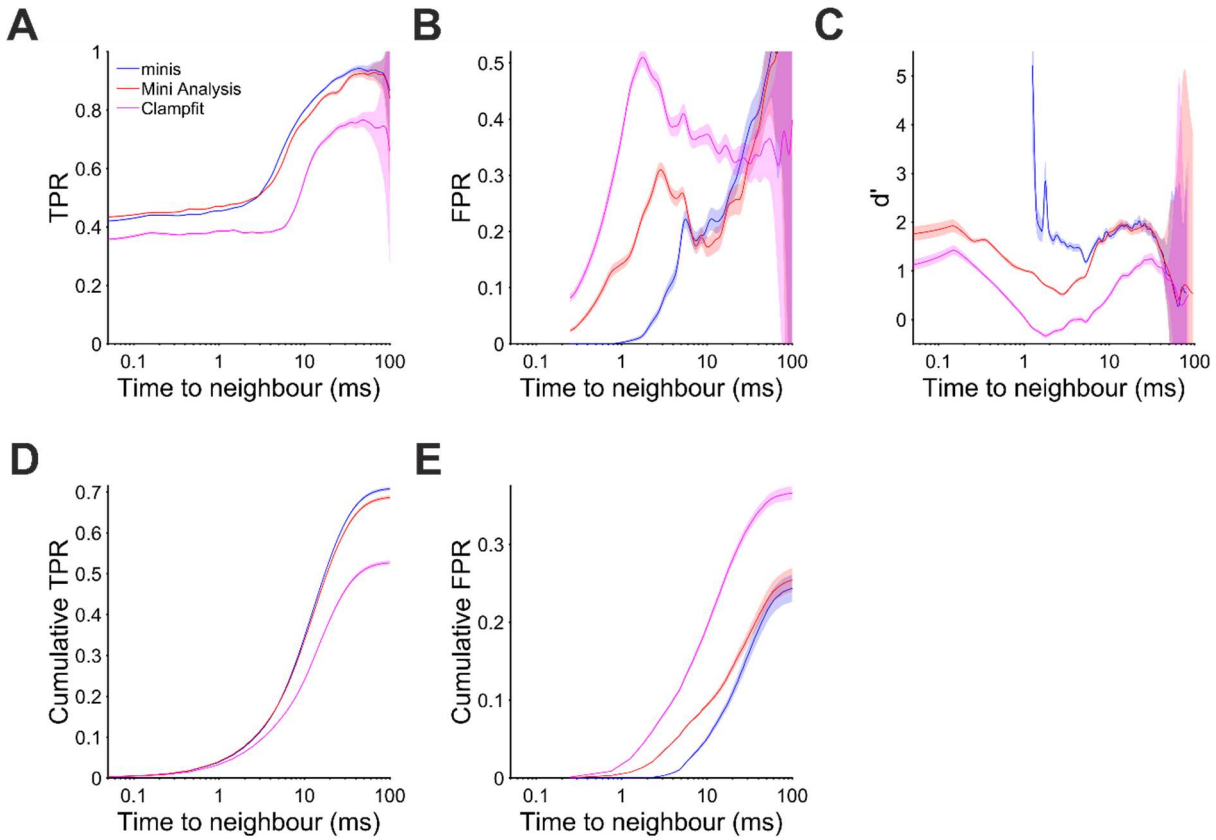

Figure 13: Performance for detecting smEPSPs of various (realistic) discrete amplitudes as a function of the time to the nearest neighbour.

(A) True positive rate (TPR) when detecting smEPSPs of various discrete amplitudes (0.05 to 0.6 mV in increments of 0.05 mV) added at random to noise waveforms, as in previous figure, as a function of the time to the nearest neighbour. Pale shaded colours indicate 95% confidence intervals.

(B) False positive rate (FPR).

(C) d' (undefined but arbitrarily high for TPR > 0 and FPR = 0, e.g. for inter-mini intervals below 1 ms, for minis algorithm).

(D) Cumulative TPR.

(E) Cumulative FPR.

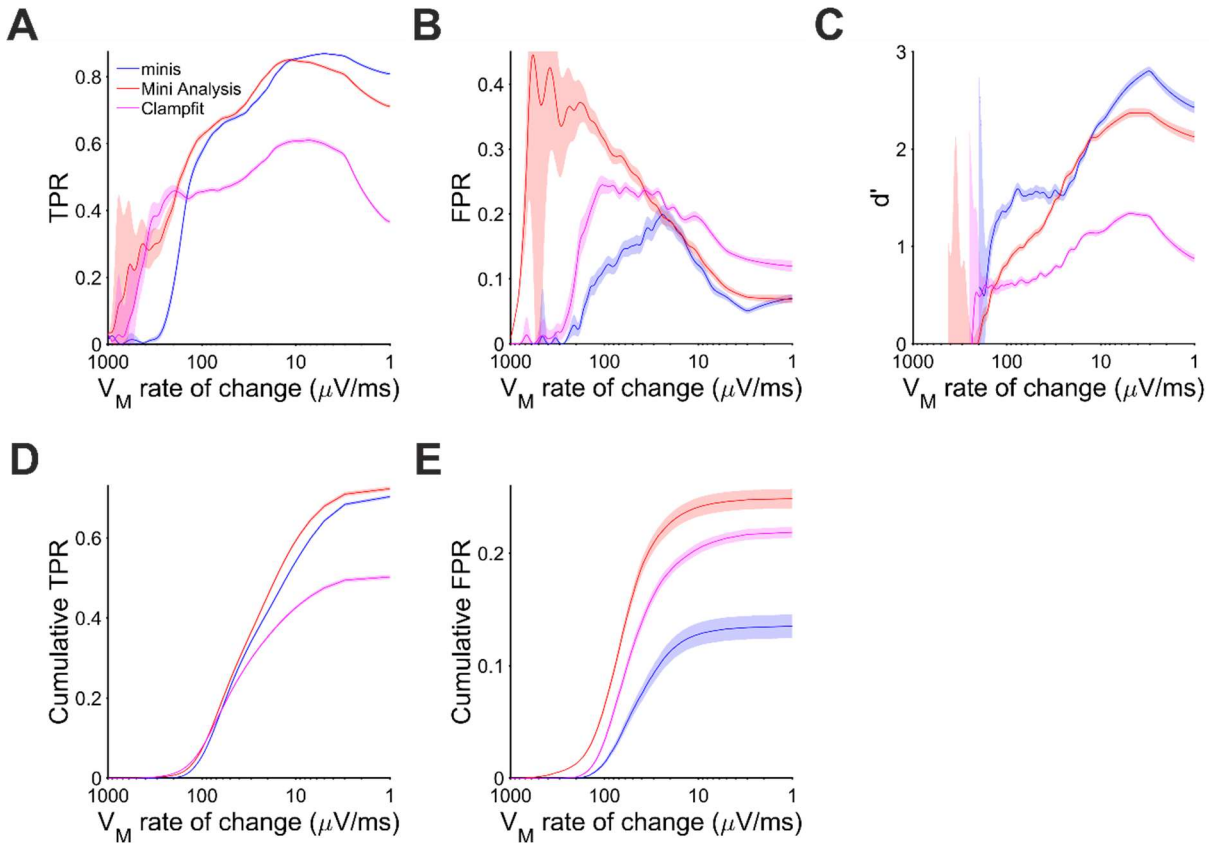

Figure 14: Performance for detecting smEPSPs of (realistic) discrete amplitudes on the membrane potential rise phase.

(A) True positive rate (TPR) when detecting smEPSPs of various amplitudes (0.05 to 0.6 mV in increments of 0.05 mV, added at random to noise waveforms, as in the previous figure), on the V_m rise phase as a function of the V_m rate of change. Pale shaded colours indicate 95% confidence intervals.

(B) False positive rate (FPR).

(C) d'.

(D) Cumulative TPR.

(E) Cumulative FPR.

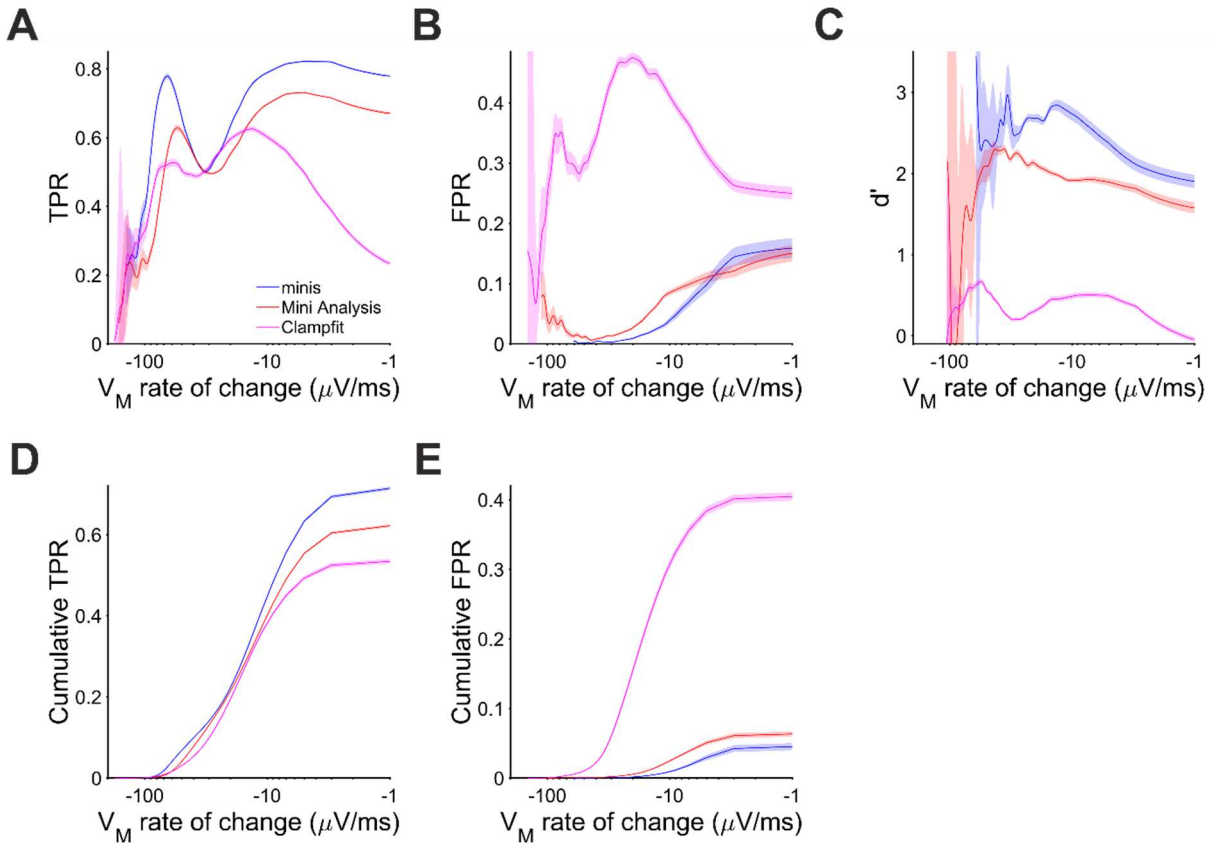

Figure 15: Performance for detecting smEPSPs of (realistic) discrete amplitudes on the membrane potential decay phase under realistic frequency conditions.

(A) True positive rate (TPR) when detecting smEPSPs of various amplitudes (0.05 to 0.6 mV in increments of 0.05 mV, as in previous figure) on the V_m decay phase, as a function of the V_m rate of change. Pale shaded colours indicate 95% confidence intervals.

(B) false positive rate (FPR).

(C) d'.

(D) Cumulative TPR.

(E) Cumulative FPR.